Resource

Cell Reports

Multiomics of synaptic junctions reveals altered lipid metabolism and signaling following environmental enrichment

Graphical abstract

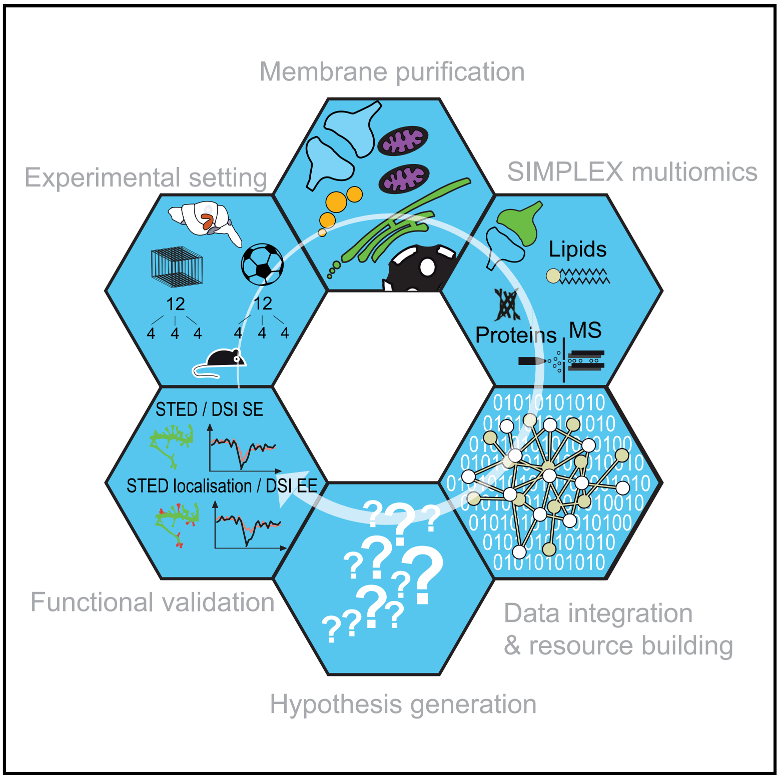

Highlights

- A multiomics workflow reveals lipid and protein networks of synaptic junctions
- An in-depth quantitative lipidome of synaptic junctions is provided
- Enriched environment reduces endocannabinoid signaling at spine synapses
- Reduced endocannabinoid signaling increases surface expression of AMPA receptors

Authors

Maximilian Borgmeyer, Cristina Coman, Canan Has, ..., Marina Mikhaylova, Michael R. Kreutz, Robert Ahrends

Correspondence

michael.kreutz@zmnh.uni-hamburg.de (M.R.K.),
robert.ahrends@univie.ac.at (R.A.)

In brief

Borgmeyer et al. provide a resource of lipid and protein content of forebrain synaptic junctions. This Multiomics is suitable to generate hypotheses on lipid signaling pathways that are altered by enriched environment in mice. The data suggest that changes in endocannabinoid signaling might affect synaptic plasticity.

Borgmeyer et al., 2021, Cell Reports *37*, 109797
October 5, 2021 © 2021 The Author(s).
https://doi.org/10.1016/j.celrep.2021.109797

CellPress

Cell Reports

CellPress
OPEN ACCESS

Resource

Multiomics of synaptic junctions reveals altered lipid metabolism and signaling following environmental enrichment

Maximilian Borgmeyer,[1,2,12] Cristina Coman,[3,4,12] Canan Has,[3] Hans-Frieder Schött,[3] Tingting Li,[3] Philipp Westhoff,[3] Yam F.H. Cheung,[3] Nils Hoffmann,[3] PingAn Yuanxiang,[2] Thomas Behnisch,[5] Guilherme M. Gomes,[2] Mael Dumenieu,[2] Michaela Schweizer,[6] Michaela Chocholoušková,[7] Michal Holčapek,[7] Marina Mikhaylova,[8,9] Michael R. Kreutz,[1,2,10,11,13,*] and Robert Ahrends[3,4,*]

[1]Leibniz Group 'Dendritic Organelles and Synaptic Function,' University Medical Center Hamburg-Eppendorf, Center for Molecular Neurobiology, ZMNH, 20251 Hamburg, Germany
[2]RG Neuroplasticity, Leibniz Institute for Neurobiology, 39118 Magdeburg, Germany
[3]Leibniz-Institut für Analytische Wissenschaften-ISAS-e.V., 44227 Dortmund, Germany
[4]Department of Analytical Chemistry, Faculty of Chemistry, University of Vienna, 1090 Wien, Austria
[5]Institutes of Brain Science, State Key Laboratory of Medical Neurobiology and MOE Frontiers Center for Brain Science, Fudan University, Shanghai 200032, China
[6]Morphology and Electron Microscopy, University Medical Center Hamburg-Eppendorf, Center for Molecular Neurobiology, ZMNH, 20251 Hamburg, Germany
[7]University of Pardubice, Department of Analytical Chemistry, CZ-532 10 Pardubice, Czech Republic
[8]Emmy Noether Group 'Neuronal Protein Transport,' University Medical Center Hamburg-Eppendorf, Center for Molecular Neurobiology, ZMNH, 20251 Hamburg, Germany
[9]AG Optobiology, Institute for Biology, Humboldt Universität zu Berlin, 10115 Berlin, Germany
[10]German Center for Neurodegenerative Diseases (DZNE), 39120 Magdeburg, Germany
[11]Center for Behavioral Brain Sciences, 30120 Magdeburg, Germany
[12]These authors contributed equally
[13]Lead contact
*Correspondence: michael.kreutz@zmnh.uni-hamburg.de (M.R.K.), robert.ahrends@univie.ac.at (R.A.)
https://doi.org/10.1016/j.celrep.2021.109797

SUMMARY

Membrane lipids and their metabolism have key functions in neurotransmission. Here we provide a quantitative lipid inventory of mouse and rat synaptic junctions. To this end, we developed a multiomics extraction and analysis workflow to probe the interplay of proteins and lipids in synaptic signal transduction from the same sample. Based on this workflow, we generate hypotheses about novel mechanisms underlying complex changes in synaptic connectivity elicited by environmental stimuli. As a proof of principle, this approach reveals that in mice exposed to an enriched environment, reduced endocannabinoid synthesis and signaling is linked to increased surface expression of α-amino-3-hydroxy-5-methyl-4-isoxazolepropionic acid receptor (AMPAR) in a subset of Cannabinoid-receptor 1 positive synapses. This mechanism regulates synaptic strength in an input-specific manner. Thus, we establish a compartment-specific multiomics workflow that is suitable to extract information from complex lipid and protein networks involved in synaptic function and plasticity.

INTRODUCTION

Synaptic junctions are the central building blocks of a chemical synapse, and compelling evidence points to an essential function of lipids in synaptic neurotransmission. Trace lipids, including phosphatidylinositol phosphates (PIP) and negatively charged phosphatidylserine (PS) are crucial for multiple steps of the synaptic vesicle cycle and vesicle fusion. Lipids also play a central role in other synaptic processes including the formation and shaping of membrane (Chernomordik and Kozlov, 2003; Puchkov and Haucke, 2013), lipid mediated signal transmission (Piomelli et al., 2007), as well as endocytosis (Kononenko and Haucke, 2015). Since most lipid mediators are direct or indirect products of polyunsaturated phospholipids, sufficient molar content of complex polyunsaturated lipids must be located at synaptic junctions to guarantee their formation (Han, 2007). In addition, several lines of evidence suggest that the lipid composition of synapses might be dynamic (Jurado et al., 2010; Martin et al., 2014). The existence of more than 40 different lipids known to modulate signaling and to influence membrane geometry of synapses and synaptic vesicles (Dieterich and Kreutz, 2016) demands a systematic large-scale study of lipid abundance and functional regulation. It is therefore not less than astonishing that neither a quantitative lipid inventory nor a detailed proteome map of the lipid metabolism of synaptic junctions are currently available.

During the past decade, mass spectrometry (MS) has evolved into a state-of-the-art technology for lipid analysis (Brügger et al., 1997; Ekroos et al., 2002; Han, 2002). The technical progress regarding sensitivity, speed, and resolution in MS (Schuhmann et al., 2012), combined with advances in systems biology (Molenaar et al., 2019), the accessibility of lipid databases and search engines (Herzog et al., 2011; Peng et al., 2020; Sud et al., 2007)—along with the availability of lipid standards for quantification nowadays—allow to address questions related to lipid function and regulation (Peng et al., 2018). Modern lipidomics tools can provide access to understand the complexity of lipids, their homeostatic regulation, and their role in neuronal plasticity, as well as diseases linked to synaptic dysfunction. In addition, evidence derived from lipidome and proteome data, if derived from the same sample, can pinpoint unexplored molecular mechanisms and interactions. Although lipidomics and dual-omics was successfully applied to image different brain regions (Ellis et al., 2018; Lerner et al., 2018), the potential of multiomics has not been used before in neuroscience to study synaptic function with purified synaptic fractions. Here, we established a multiomics extraction strategy (Coman et al., 2016) and quantitative mass spectrometry workflow to determine the lipid inventory and metabolic proteome of forebrain synaptic junctions. We then executed the workflow on mouse hippocampal synaptic junctions to monitor alterations of lipid metabolism and signaling induced by an enriched environment (EE). Finally, based on multiomics and subsequent bioinformatic analysis we generated a hypothesis on a molecular mechanism that might contribute to changes in synaptic plasticity elicited by environmental stimuli.

RESULTS

Quantitative multiomics of synaptic junctions

For multiomics method development, hippocampal tissue from rat brain was used as a starting material, considering the higher sample yield. We enriched rat forebrain synaptic junctions (SJ) utilizing sucrose density gradient fractionation (Wendholt et al., 2006) and used a multiomics mass spectrometry–based workflow to determine their general molecular composition (Coman et al., 2016; Figures S1A–S1C). This preparation contains proteins of all compartments contributing to the synaptic junction including the postsynaptic density (PSD), the presynaptic cytomatrix of the active zone (CAZ), the synaptic extracellular matrix (perisynaptic extracellular matrix and synaptic cleft ; for review see Dieterich & Kreutz, 2016), as well as synaptic membranes from where lipids were not extracted with detergents. The sample preparation for shotgun lipidomics and endocannabinoid and sphingolipid analysis required 300 μg of a synaptic protein preparation. In brief, MeOH was added to the sample, and three freeze-thaw cycles with intermediate ultrasonication were necessary to homogenize the sample. Next, methyl-tert-butyl-ether and the internal standard mixture were added, and the samples were incubated for 1 h at 950 rpm and 4°C. To induce phase separation, water was added to the samples. After a centrifugation step of 10 min at 4°C and 10 000 g, the upper organic phase (containing phospholipids [PLs], sphingolipids [SLs], sterols [ST] and glycerol lipids [GLs]) was carefully removed and dried under a gentle nitrogen flow whereas, to the lower aqueous phase, methanol was added. Subsequently, the samples were stored at −20°C for 2 h to complete protein precipitation and centrifuged for 30 min at 13 500 g. The protein pellet was dried and further subjected to protein analysis and the dried organic phase was reconstituted for lipid analysis as previously described (Coman et al., 2016).

The lipid-category tailored extraction procedures allowed simultaneous protein sample preparation (Figures 1A–1F). We utilized internal lipid standards at species- or lipid-class level to obtain an absolute quantification of lipids. For protein analysis, a Tandem Mass Tags (TMT)-based labeling approach was employed to increase identification and quantification accuracy. The mass spectrometry-based global proteomics analysis was integrated with top-down shotgun and targeted lipidomics to establish a multiomics workflow (Figures 1B–1D). In total, 5,248 proteins were quantified in all fractions by nanoLC-high resolution mass spectrometry (Figure 2A; Tables S1Aand S1B) ranging from low abundant proteins such as Neu4 (Neuraminidase 4) to high abundant molecules such as voltage-dependent anion channel 1 (VDAC1). Overall, the abundance of 3,580 proteins was determined to be statistically significant different in all three analyzed fractions (Figure 2B). When we filtered by a fold change threshold 447 proteins were depleted > 2-fold and 126 proteins were enriched < 2-fold from the heavy membrane fraction to synaptic junctions (Tables S2 and S3). A cellular component related GO-term (Gene Ontology) enrichment analysis (Figure 2C) revealed an enrichment of proteins related to the term's synaptic vesicle, pre- and postsynaptic region, as well as transporters and receptors. The proteome of this study yielded a coverage of 91% and 70% in comparison to previously reported synaptosome proteomes (Figure 2D; Biesemann et al., 2014; Heo et al., 2018). Moreover, we reached 77% coverage of the SynGo database (Table S2), an expert curated database of synaptic proteins (Koopmans et al., 2019), which is twice the coverage of earlier reports.

The lipid inventory of synaptic junctions

The novel multiomics strategy revealed the presence of synaptic junction–associated proteins that are involved in lipid metabolism (Figure 3F). We found molecules derived from the fatty acid synthesis pathway, glycerol, and glycerophospholipid metabolism; and we also identified many proteins involved in sphingolipid and endocannabinoid metabolism (Figure S2). In total, 923 proteins and lipids (Table S4) establish this network, indicating that the synaptic junction harbors a highly diverse repertoire of lipid metabolic capacity.

For confident identification of lipids, all lipid molecules were structurally characterized by tandem mass spectrometer analysis (MS/MS) monitoring multiple fragments per lipid species (Figure S3). The procedure allowed structural characterization of lipids at the fatty acid (FA)-species level with high confidence, with the definition of the number of double bonds and carbon atoms for each FA chain (Figure S3A–S3E). This information is of critical importance, since the chain length and the number of double bonds were shown to have a fundamental effect on

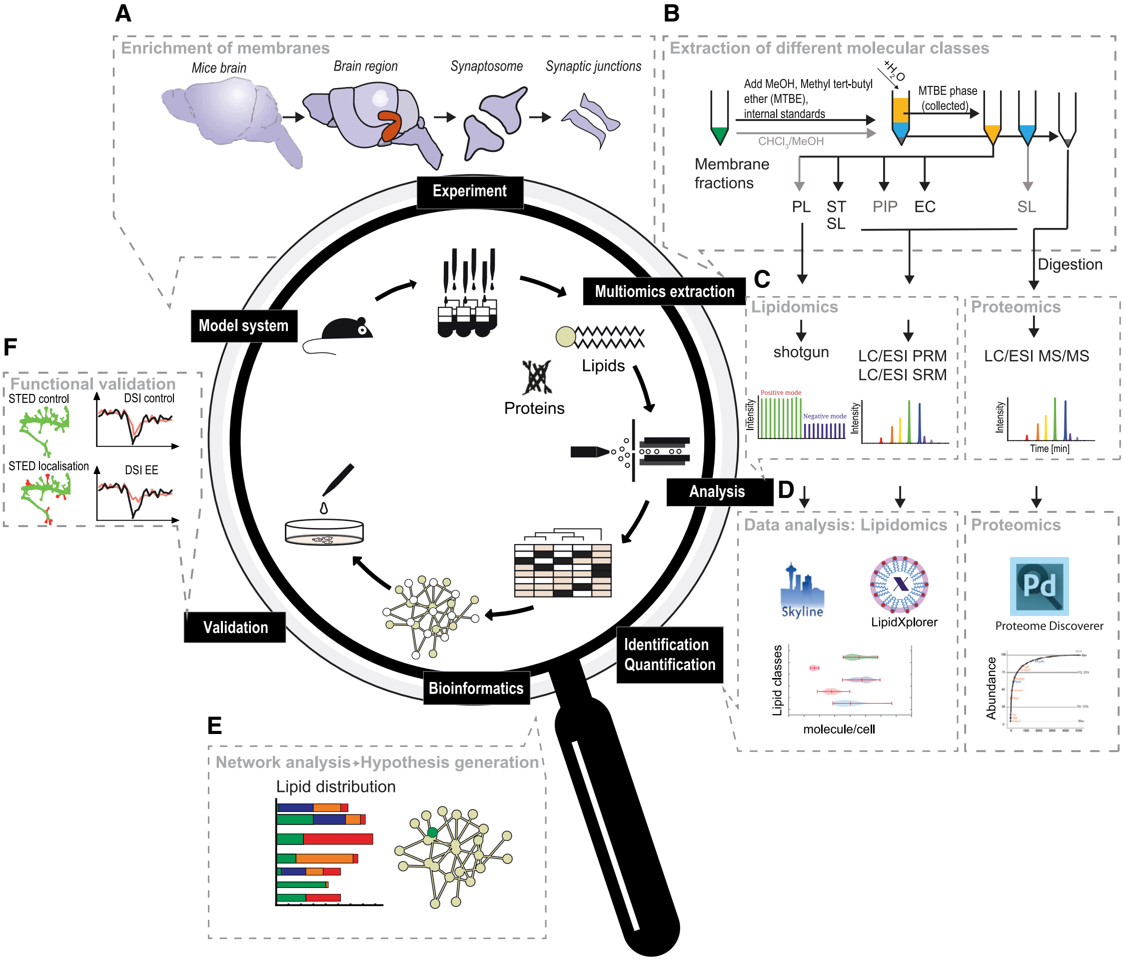

Figure 1. Comprehensive multiomics analysis of synapse compartments

(A) Isolation and purification of organelles from rodent models.

(B) Lipid extraction and internal standard addition applied to lipid-category tailored analysis. Proteins are hydrolyzed and subjected to tandem mass tag labeling.

(C) Lipid and protein analysis by shotgun or targeted MS/MS analysis.

(D) Lipidomics and proteomics data analysis. The structural characterization of lipids by LipidXplorer or Skyline, followed by absolute quantification of all detected lipid species. The proteins were identified with an FDR $\leq$ 1% and quantified using Proteome Discoverer.

(E) Establishment of a lipid-protein matrix to form a lipid network. Elucidation of EE-specific differences identified from quantification of proteins and lipids.

(F) Validation by additional in-vitro and *ex vivo* experiments, including functional assays. Chloroform (CHCl3), methanol (MeOH), phosphoinositides (PIP), methyl tert-butyl ether (MTBE), sterols (ST), sphingolipids (SL), phospholipids (PL), endocannabinoids (EC), glycosphingolipids (GSL), liquid chromatography (LC), electrospray, (ESI), parallel reaction monitoring (PRM), selected reaction monitoring (SRM), mass spectrometry (MS), stimulated emission depletion microscopy (STED), Depolarization-induced suppression of inhibition (DSI), falls discovery rate (FDR).

neurotransmission and synaptic function (Soni et al., 2008). Additionally, the lipid FA composition contributes to physicochemical properties of the membrane, including stiffness, thickness, and lateral diffusion of membrane components (Antonny et al., 2015; Lauwers et al., 2016).

The lipidome analysis structurally characterized and identified 416 lipid species (Figures 3A 3E; Table S5) originating from the main lipid categories PL (253), GL (12), SL (58), endocannabinoids (EC, 26), GSL (60) and Chol and STE (6), thereby covering 49 different lipid classes (Table S5). Following lipid identification, quantitative analysis across heavy membranes, synaptosomes, and synaptic junctions were executed using lipid-class/species-specific internal standards. The heavy membrane or P2 fraction contains the synaptic plasma membrane and synaptosomes can be isolated by ultracentrifugation on a sucrose density gradient from this fraction. Synaptic junctions result from osmotic lysis of synaptosomes and are largely devoid of synaptic vesicles, and contain less mitochondria. We further assessed synaptic junction abundance and distribution of all quantified lipids at the category and class level (Figures 3A and 3B). The concatenation of lipidomics data which is derived from different analysis strategies can be realized by a quantitative reporting utilizing internal standards. Quantifying the bulk of membrane lipids but also reporting rare signaling molecules such as endocannabinoids or PIPs as part of the lipidome is important to understand their relations within the synaptic compartment. Hence,

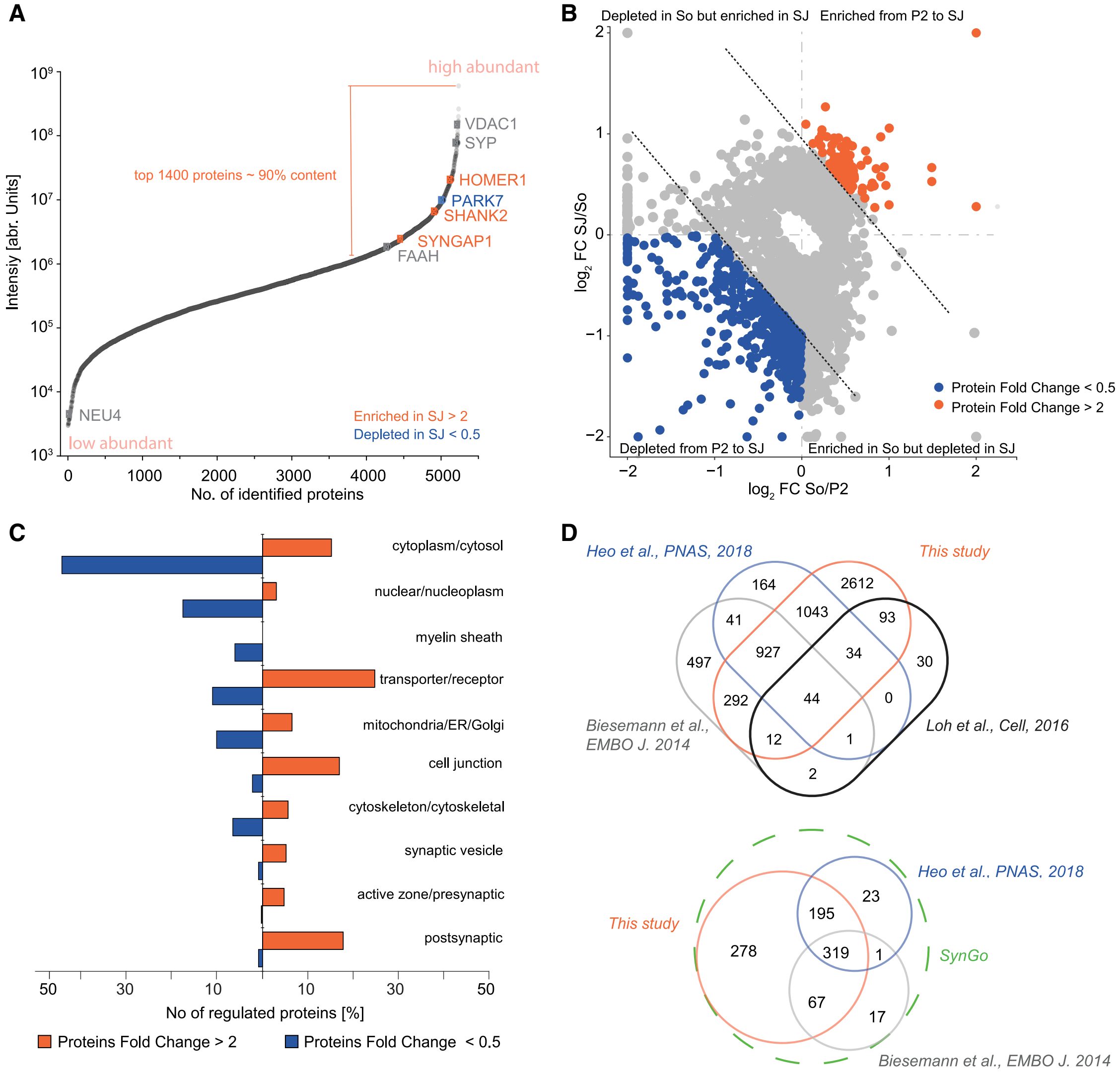

Figure 2. The global quantitative proteome of rat hippocampal synaptic junctions

(A) Global proteomics analysis of hippocampal membrane (P2), synaptosome (So) and synaptic junction (SJ) fractions. The dynamic range of proteins of the SJ fraction is depicted according to mass spectrometry derived, summed up peptide intensities. The most abundant 1400 proteins make up to 90% of the total protein content. Proteins of interest which have statistical significance ($p < 0.05$) and a foldchange above 2 were classified as enriched (orange) and depleted (blue) for SJ in comparison to P2 or are indicated in gray if they were not regulated across the fractions.

(B) Sector plot showing log2 fold change of statistically significant proteins ($p \leq 0.05$). Proteins are classified as depleted or enriched based on log2 fold change threshold. The statistical significance was calculated based on one-way ANOVA test followed by Benjamini-Hochberg correction. Among significant proteins (gray), depleted proteins whose expressions are decreasing from P2 to SJ continuously are shown as blue, enriched proteins whose expressions are increasing from P2 to SJ are shown as orange.

(C) Gene ontology terms from cellular components associated with the enriched (orange) and depleted (blue) proteins in the SJ compared to P2. The percentage of proteins associated with the indicated cellular components was calculated based on the total number of enriched or depleted proteins.

(D) Venn diagram of shared and unique proteins between recent synaptic junction proteome studies and the analyses carried out here (left) and the protein coverage as compared to SynGO, a synaptic gene ontology data base (right).

All data are combined from 3 independent biological experiments ($n = 3$), and mean values are shown, error is displayed as standard deviation, $p \leq 0.05$. See also Figure S1.

concatenating the quantitative results revealed a high dynamic range of lipid species greater than 7 orders of magnitude (Figure 3A; Table S5). Interestingly, 75% of the total junction lipid content is made up out of only 15 lipid species at which over 50% carrying one polyunsaturated fatty acid (PUFA; C20:4, C22:4 and C22:6) (Figure 3C). PUFA-phospholipids (PUFA-PLs) are enriched in the synaptic membrane facilitating presynaptic functions and membrane remodeling (Lauwers et al., 2016). Comparing the heavy membrane fraction to the synaptic junction fraction reveals the enrichment and depletion of distinct

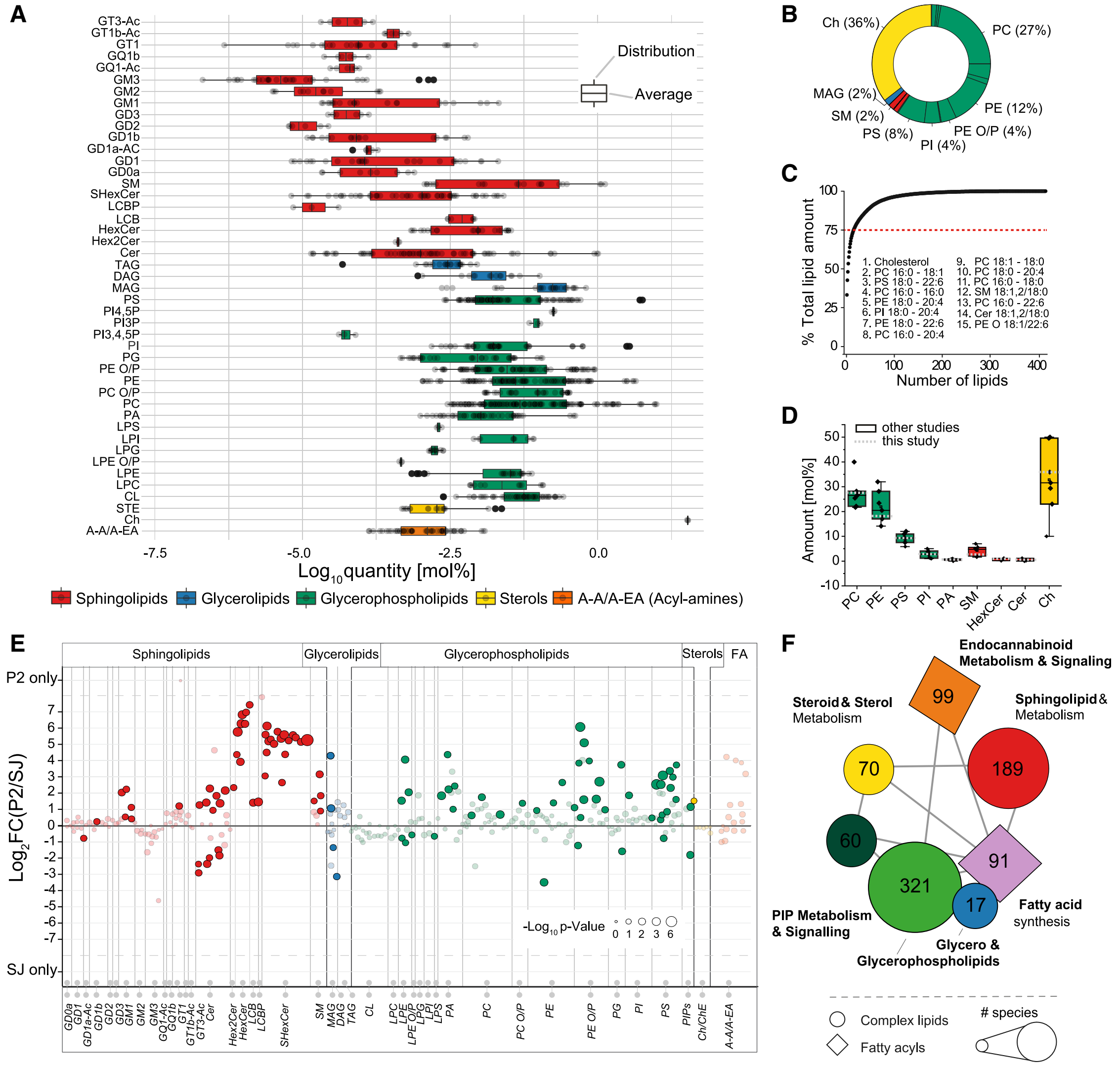

Figure 3. Quantitative lipid inventory analysis of synaptic junctions indicates a large concentration range of lipid species and reveals lipid-related synaptic junction signatures

(A) Boxplots displaying the dynamic range of the synaptic junction lipidome from hippocampal rat brain. Five lipid categories (glycerolipids, glycerophospholipids, sphingolipids, sterols, and aminoacyls) spanning over a total of 45 lipid classes and 416 lipid species are shown in molar percentage. Abbreviations are given in Table S10.

(B) Distribution of lipid classes determined in synaptic junctions. Lipid classes are denoted by category.

(C) Cumulative lipid abundance, 15 species contribute to 75% of the total lipid content of the synaptic junctions.

(D) Boxplots at the lipid class level in comparison to earlier reports on major lipid classes (Benfenati et al., 1989; DeVries et al., 1981; Nagy et al., 1976; Takamori et al., 2006; Walker and Agoston, 1987). Boxplot shows the median with whiskers from minimum to maximum.

(E) Bubble plot of lipid species separated by lipid category displays enriched and depleted lipids at the synaptic junction as compared to the heavy membrane fraction (abbreviations in Table S10).

(F) Lipid related network mapping shows the quantified lipid related enzymes and quantified lipids that are significantly enriched or depleted as compared to other fractions. Significantly enriched and depleted proteins were queried against KEGG databases and KEGG annotated enzymes were mapped to "Metabolism of lipid" related subpathways such as glycerophospholipid and glycerolipid metabolism pathways.

All data are combined from 3 independent biological experiments (A) or 5 previously published reports (D), and mean values are shown. In A, and D, data are presented as boxplots with whiskers from minimum to maximum. A Student's t test was used for the statistical testing with the following parameters: two-sided, true variance equality and confidence level at 0.95.

See also Figures S2 and S3.

lipid classes and species. Ceramides (Cer) are enriched in junctions whereas dihexosyl ceramides (DiHexCer), hexosyl ceramides (HexCer), sulfatides (SHexCer), which are usually found in high concentration in the myelin sheath are depleted (Figure S4). However, in the most abundant lipid classes phosphatidylcholine (PC) and phosphatidylethanolamine (PE), only a minority of species are altered indicating that the junction-specific lipid composition is primarily determined by sphingolipids and cholesterol (Figures 3D and 3 E; Figure S4A), the key components of lipid microdomains. Notably, the concentration of cholesterol is remarkably decreased in synaptic junctions compared to P2 ($\geq 1.1x10^{-6}$ mol/mg$_{Protein}$ (Figure S4A, B)).

Besides the analysis of structural membrane lipids, we also analyzed signaling lipids such as phosphoinositides and endocannabinoids which are based on their chemical nature hard to detect, or are very low abundant and only detectable by an adaptation of workflows. Moreover, we were able to quantify different phosphoinositides classes (PIP, PIP2 and PIP3) with isomer resolution (Figures S4A and S4B). Phosphoinositides were detected in concentration ranges from $1.1x10^{-9}$ for PI(4) P down to $7.2x10^{-13}$ mol/mg PI(3,4,5)P3. Whereas the PI(4)P concentration is increased in the synaptic junction, the PI(4,5) P2 and PI(3,4,5)P3 concentrations are reduced by half, which correlates with decreased levels of their generating enzyme PI3-Kinase and steady-state levels of the degradative phosphatase PTEN (Table S6; Rusten and Stenmark, 2006).

Enriched environment impacts hippocampal endocannabinoid signaling (ECS)

Several lines of evidence indicate that the lipid composition of the synapse is dynamic (Jurado et al., 2010; Martin et al., 2014; Tulodziecka et al., 2016). Early exposure of mice to EE promotes synaptic plasticity in the hippocampus and enhances cognitive function (Ohline and Abraham, 2019). With respect to the lipid inventory of synaptic junctions, the identified lipid species across the different lipid categories were very similar in mouse and rat and shared a significant proportion (Figure S4C). The most abundant molecules were identical and determined in average 80% of the lipid class membrane composition. We therefore wondered whether the established method is sensitive enough to reveal the probably subtle effects of environmental stimuli like housing conditions on the molecular composition of hippocampal synaptic junctions (Figure S5A). Multiomics of synaptic junctions from mice subjected to EE as compared to standard environment (SE) revealed 178 proteins and 20 lipids to be significantly regulated ($p \leq 0.05$) (Figures 4A–4C). In this set, we found 57 proteins to be upregulated and 121 proteins to be downregulated (Figure 4A; Table S7). Overall, 17 lipids were significantly downregulated and 3 upregulated (Figure 4B; Table S7). This accounts approximately for a change of only 0.1 mol % of the entire SJ lipidome, indicating that no major membrane remodeling of hippocampal synapses occurs in response to EE which is in accord to previous literature (Reichmann et al., 2015) and indicates that main structural lipids will not contribute to alterations in synaptic function in EE=housed mice. An unbiased protein ontology enrichment analysis (Figure 4D) revealed that 26 pathways related to synaptic plasticity are regulated including retrograde endocannabinoid signaling (Figure 4D, upper inlet). This was underscored by a lipid ontology enrichment analysis where lipid terms of this pathway were clearly enriched (Figure 4D, lower inlet). At the protein level, two proteins of the endocannabinoid signaling pathway, ABHD6 (Monoacylglycerol Lipase) and FAAH (Fatty Acid Amide Hydrolase) are down or upregulated by 45 and 35%, respectively (Figure 4A; Figure S5B). Accordingly, we found increased FAAH-activity in synaptic protein fractions prepared from mice raised in EE (Figure 5E). These changes are accompanied by changes in the concentrations of the endocannabinoid (EC) messenger 2-AG (2-Arachidonoylglycerol) (Figure 4E) as well for its precursors such as DAG 38:4 which are significantly decreased (Figure 4B). However, protein levels of the endocannabinoid receptor (CB1R) and hydrolases such as MAGL were unaffected in EE. These findings prompted us to underscore the potential of the workflow to discover novel mechanisms with a more detailed analysis of altered ECS in mice subjected to EE (Figure 4F).

Altered ECS in response to enriched environment is restricted to Schaffer collaterals

To exclude the possibility that gross alterations in structural connectivity account for the proteomic changes in mice subjected to EE, we initially analyzed synapse number and structure with electron-microscopy (EM) in the CA3 region and the strata oriens and radiatum of the CA1 region. This analysis revealed no significant differences in spine number and the length of the postsynaptic density (PSD) (Figures S5C–S5K). In addition, we found no change in the number of mitochondria in these hippocampal subfields (Figures S5G, S5K, and S5O), indicating that any regulation of ECS is not easily explained by the presence of an increased number of mitochondria, which express high levels of CB1R (Bénard et al., 2012). Depolarization-induced suppression of inhibition (DSI) is a classical form of short-term synaptic plasticity of GABAergic transmission that crucially relies on endocannabinoids as the retrograde messengers responsible for its induction (Augustin and Lovinger, 2018). A subsequent patch-clamp experiment indeed revealed a reduced magnitude of DSI in CA1 pyramidal neurons of mice raised in EE (Figures S5P and S5Q), a result that confirms reduced retrograde ECS at GABAergic synapses in the hippocampus.

In accordance with the proteome analysis, levels of ABHD6 were reduced while those of FAAH were elevated in immunoblotting experiments of hippocampal synapse–enriched fractions obtained from EE mice (Figures 5A–5D). However, it turned out that neither FAAH nor ABHD6 are present at inhibitory synapses that were identified by immunostaining with an antibody directed against Gephyrin (Figures S6A–S6D). In contrast, we observed extensive co-localization of both proteins with Shank3 positive spine synapses in CA1 and CA3 pyramidal neurons in accord with previous findings (Figures 5E–5M) (Gulyas et al., 2004; Marrs et al., 2010). A quantitative analysis revealed a significant down- and vice versa upregulation of ABHD6 and FAAH at excitatory synapses of the stratum radiatum and stratum oriens but not the stratum lacunosum moleculare (Figures 5G–5N). Thus, changes in protein expression are confined to connections of CA1 with presynaptic terminals of CA3 neurons via Schaffer collaterals.

Postsynaptic ABHD6 and FAAH expression depends on ECS and synaptic activity

Collectively these results suggest that EE might also have impact on retrograde ECS at excitatory synapses. In the hippocampus CB1R are predominantly expressed at inhibitory terminals and only a subset of excitatory synapses (Katona and Freund,

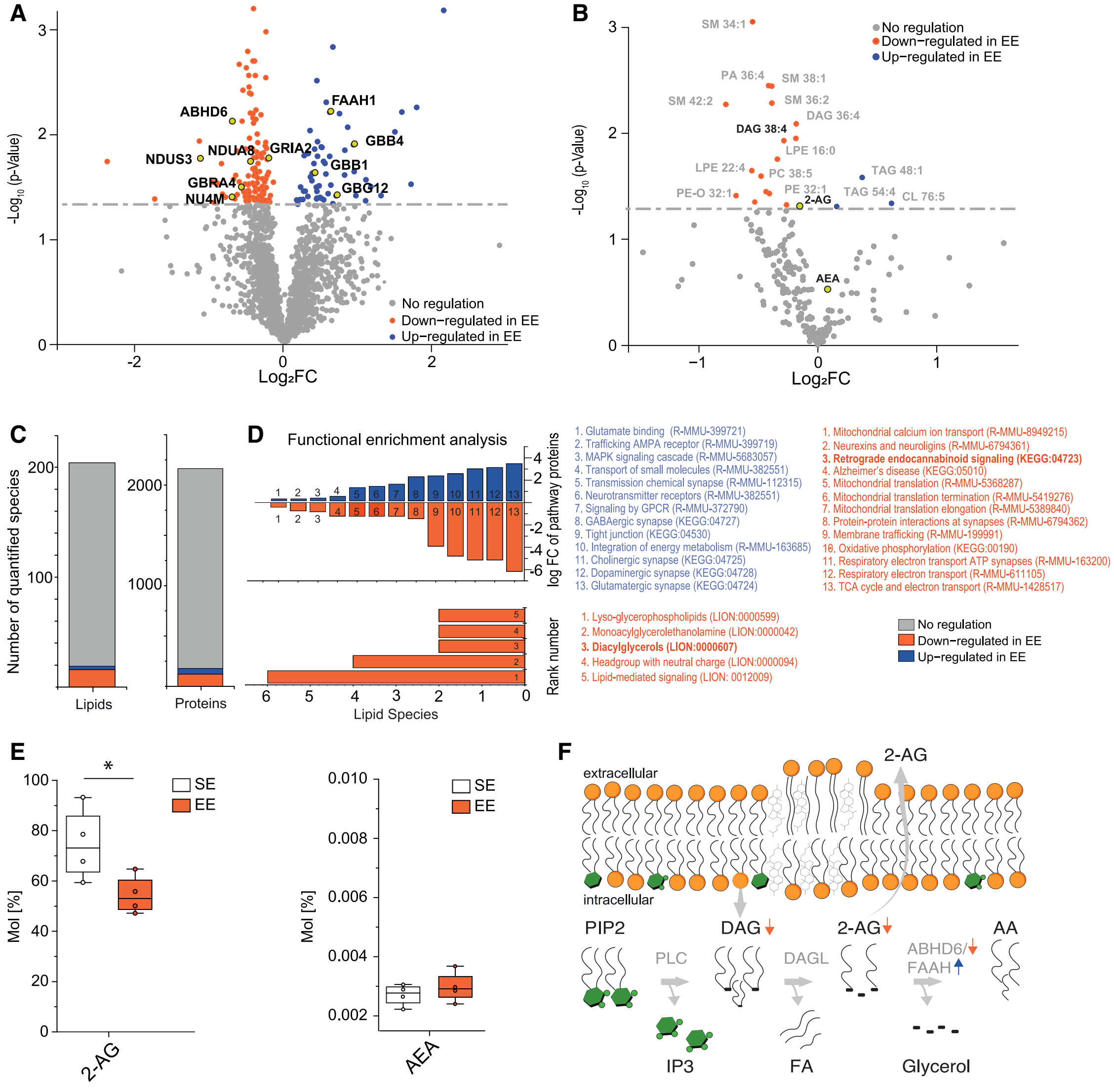

Figure 4. Multiomics analysis reveals regulation of endocannabinoid signaling in enriched environment

(A) Volcano plot of $\log_2$ fold changes of proteins in hippocampal synaptic junctions of mice raised in EE. Downregulated species (orange), upregulated species (blue) and non-regulated lipids (gray). Global proteomics analysis identified 2164 proteins from which 57 and 121 revealed a significant up- or downregulation, respectively. Significant changes in the proteome are indicated by minimum $\log_2$-fold change with $p \leq 0.05$. Identified proteins of the retrograde endocannabinoid pathway were identified and individually labeled.

(B) Volcano plot of $\log_2$-fold changes of lipid species concentrations in hippocampal synaptic junctions of mice housed in EE. Global lipidomics analysis identifies 23 regulated lipids. In red: downregulated species, upregulated species (blue) and nonregulated lipids (gray). 2-AG, 2-arachidonoyl glycerol, 1-AG, 1-arachidonoyl glycerol and AEA, N-arachidonoyl ethanolamide (anandamide) are indicated.

(C) Number of downregulated (orange) or upregulated (blue) lipids and proteins in EE.

(D) Ontology enrichment for proteins and lipids was conducted according to previously published reports (Jassal et al., 2020; Kanehisa et al., 2016; Molenaar et al., 2019b).

(E) Boxplots of ECs display a significant reduction of the main endocannabinoid signaling lipid 2-arachidonoyl glycerol whereby N- arachidonoyl ethanolamine remained unchanged in synaptic junctions of mice raised in EE. Boxplot shows the median with whiskers from minimum to maximum.

(F) The 2-AG synthesis branch of the retrograde endocannabinoid pathway is depicted.

All data are combined from 4 independent biological replicates. One biological replicate was comprised out of 8 individual animals. Mean values are shown, error bars represent standard deviation, $p \leq 0.05$.

See also Figure S4.

2012; Marrs et al., 2010). The number of CB1R containing synapses was not changed in response to EE (Figures S6E–S6H). Drugs known to prevent the activation of CB1R or to inhibit the synthesis of 2-AG, the predominant endocannabinoid in the hippocampus, cause enhanced long-term plasticity (LTP) that is induced by a weak-θ-burst stimulation, thus suggesting that

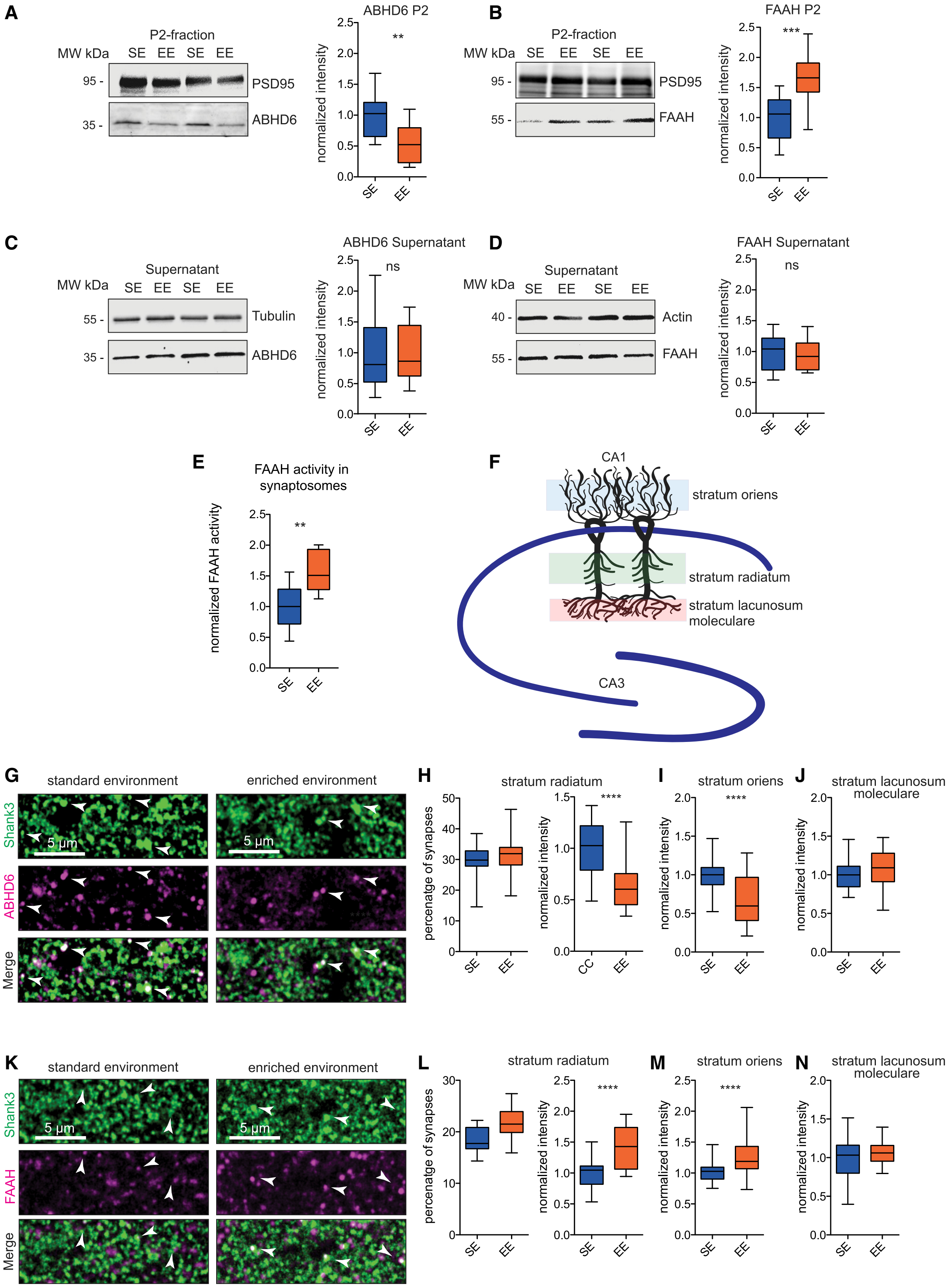

(legend on next page)

endocannabinoids regulate this form of plasticity (Augustin and Lovinger, 2018). The CB1R antagonist ribmonabant indeed attenuated the field excitatory postsynaptic potential (fEPSP) slope following the induction of this type of LTP in slices from SE mice whereas the opposite was found in slices from EE mice (Figures 6A–6C). Thus, ECS seems to be altered following EE at a subset of excitatory CA1-CA3 synapses in a plasticity-relevant manner.

What could be a potential mechanism behind these findings? Like in hippocampal brain sections, only 30% of all synapses were positive for ABHD6 and FAAH in hippocampal primary neurons, and these synapses were always in apposition to CB1R-positive boutons (Figures S7A–S7H). Most important, MAGL the major catabolizing enzyme for 2-AG is only expressed in axons but not present in dendrites and spines (Figures S7I and S7J). Since the antibodies for ABHD6 and FAAH were generated in the same species, we could not perform a co-localization study, but given that they show a similar distribution profile with respect to presynaptic CB1R, we assume that they are both present in the same synapses. Two-color STED imaging revealed clusters of ABHD6 in a subset of dendritic spines labeled with the excitatory synapse marker Shank3 (Figure 6D). Interestingly, ABHD6 showed a prominent localization in spines containing endoplasmic reticulum as evidenced by the association with the spine apparatus labeled by Synaptopodin (Figures 6E–6G). Thus, the majority of CB1R positive synapses will contain a postsynaptic spine apparatus that serves as an intracellular Ca^{2+}-store.

We next asked whether altered synaptic activity, which is a likely consequence of EE, is a driving force for the postsynaptic localization of both enzymes. Silencing of cultures with a bath application of tetrodotoxin led to a reduced expression of FAAH at postsynaptic sites, while the postsynaptic localization of ABHD6 was not affected (Figures 6H 6K). In previous work it was shown that presynaptic CB1R signaling stimulates, as part of a positive feedback loop, the postsynaptic production of 2-AG (Anderson et al., 2015). When we applied the CB1R antagonist AM-251 we observed that the synaptic localization ABHD6 was significantly reduced, whereas that of FAAH was not affected (Figures 6L 6O), suggesting that ABHD6 needs 2-AG production for its postsynaptic localization. ABHD6 is an ER-resident enzyme and most interestingly, its reduced postsynaptic localization following blockage of CB1R came along with a displacement of the Synaptopodin-positive spine apparatus (Figures 6P–6Q). Thus, most likely, a retraction of ER-membranes from spines of CB1R bearing synapses underlies the removal of ABHD6 from synapses in response to reduced ECS. Collectively, these findings open an interesting scenario. ABHD6 has a second cellular function as an auxiliary subunit of AMPAR that negatively controls surface expression of GluA1 (Wei et al., 2016). We indeed found that shRNA knockdown of ABHD6 in hippocampal primary neurons resulted in increased surface expression of GluA1 exclusively at CB1R positive synapses (Figures 7A and 7B; Figures S7E–S7H). When we enhanced synaptic activity in primary neurons with bicuculline and 4-aminopyridine, we observed following blockage of presynaptic CB1R with AM-251, conditions under which postsynaptic ABHD6 protein levels are low, and increased surface expression of GluA1 at CB1R positive synapses (Figures 7C–7E). These findings were further corroborated by immunofluorescence staining of GluA1 in brain sections of mice subjected to EE (Figures 7F–7I). Here we found increased immunofluorescence intensity of GluA1 only at synapses in the stratum oriens and radiatum that were positive for CB1R (Figures 7F–7H) but not in the stratum moleculare lacunosum (Figure 7I).

DISCUSSION

In recent years, a few studies tried to shed light on different aspects of the brain lipidome. Many of them did not elucidate the chemical nature of the described individual lipids and rather report the lipidome as a compilation of lipid features, which are uncharacterized ions in the gas phase derived from liquid-liquid extraction presumably containing lipids. Other studies used the potential of MS and bioinformatics based lipidomics, and delivered true lipid identities at the molecular lipid level (e.g., of different brain regions [Almeida et al., 2015; Fitzner et al., 2020; Yu et al., 2020]). However, to investigate the role of lipids in synaptic function, a number of aspects had to be considered such as the analysis of purified compartments, the use of detergent-free conditions to analyze the membrane of interest after purification, and reporting of concentration to understand the dimensions of membrane rearrangement under the given circumstances.

Figure 5. Immunoblotting and immunohistochemical analysis reveals altered hippocampal expression of ABHD6 and FAAH at Schaffer-collateral synapses in mice raised in EE

(A and B) Blots of the P2-fraction and the supernatant of 14 EE and 14 control animals. Blots were processed with antibodies directed against ABHD6 (A), FAAH (B) and PSD95 (A and B) as loading control. ABHD6 and FAAH immunoreactive bands were normalized to PSD95.

(C and D) Blots of the supernatant were probed with ABHD6 (C) and FAAH (D), beta-Tubulin and beta-Actin antibodies, respectively. ABHD6 was normalized to β-Tubulin and FAAH to β-Actin.

(E) FAAH activity in hippocampal synaptosomes prepared from mice raised in SE and EE. N:8 animals in each group.

(F) Overview of the hippocampus. Areas of CA1 that were analyzed with IHC are highlighted.

(G–H) Cryosections from animals raised in SE or EE (four in each group) were analyzed for ABHD6 and Shank3 immunofluorescence. Images were acquired in the stratum radiatum (G and H), stratum oriens (I) and stratum lacunosum moleculare (J), scale bar is 5 μm. Intensity of the ABHD6 staining was measured for ABHD6 puncta colocalizing with the synaptic marker Shank3. Colocalization is indicated by arrows.

(K–N) Cryosections from animals raised in SE or EE (four in each group) were analyzed for FAAH and Shank3. Images were acquired in the stratum radiatum (K and L), stratum oriens (M), stratum lacunosum moleculare (N), scale bar 5 μm. Intensity of the FAAH staining was measured for FAAH puncta colocalizing with the synaptic marker Shank3. Colocalization is indicated by arrows.

Data are presented as boxplots with whiskers from minimum to maximum. ****$p \leq 0.0001$ (Student's t test), ns $p > 0.05$.

See also Figure S5.

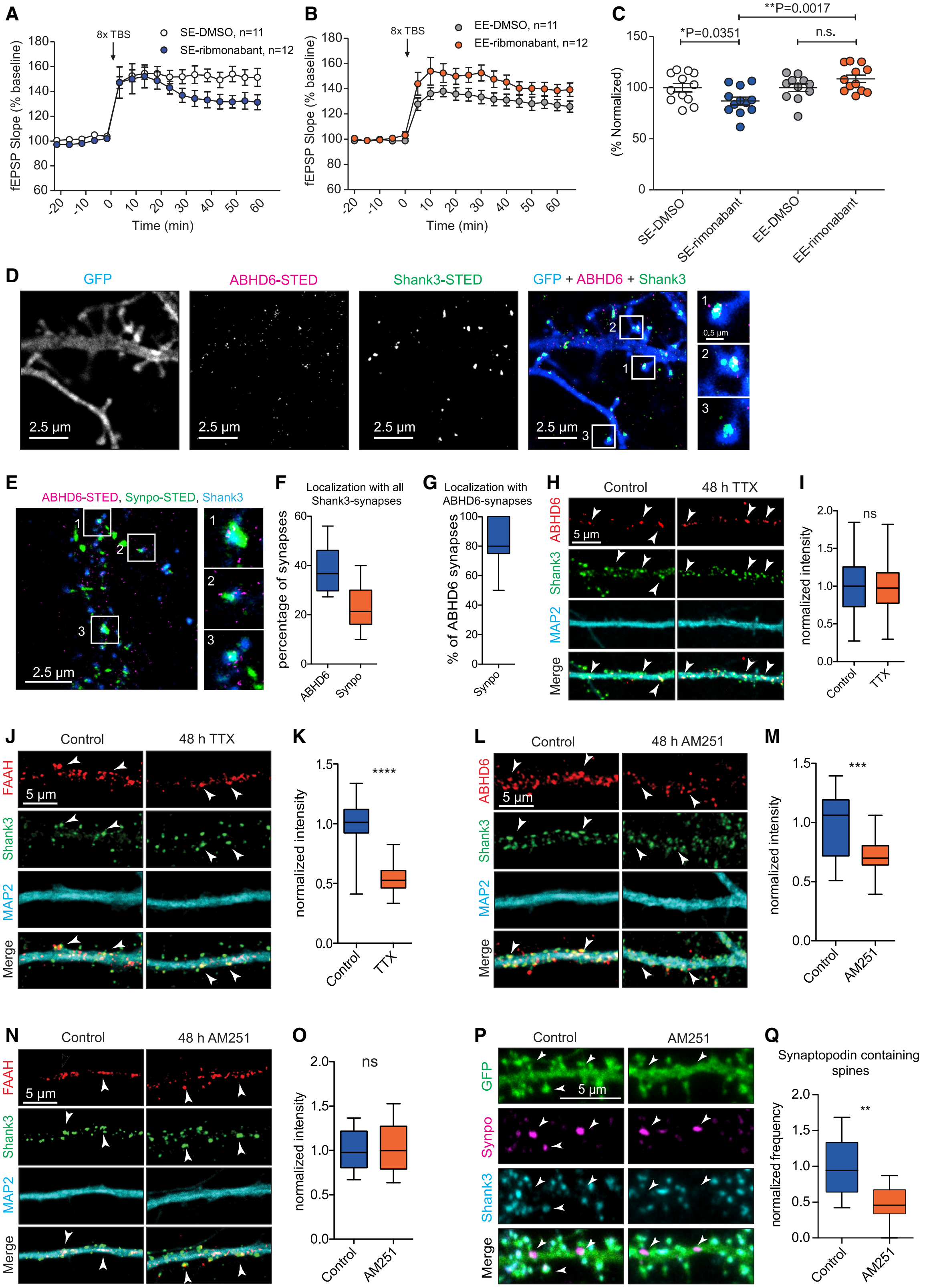

(legend on next page)

We have used the full technological advance of MS-based lipidomic analysis to determine the synaptic lipidome, and a concurrent proteome analysis deciphered the lipid metabolic capacity of synaptic junctions. Studies on synaptic lipid composition and metabolism are sparse and the feasibility of multiomics workflows to study synaptic function has not been tested yet. We extracted and analyzed from one sample different molecule classes and provide with a concatenated quantitative workflow a comprehensive quantitative lipid inventory of the rodent synaptic junction. We quantified 416 lipid species covering a concentration range over seven orders of magnitude and, in parallel, expression levels of over 5428 proteins were determined. Using one sample to cover multiple molecule classes reduces the analytical error and enhances the correlation between different molecules (Coman et al., 2016). Therefore, this analysis permitted a more precise systematic assessment of the lipid metabolic network in synaptic junctions where 923 molecules were identified in lipid metabolic networks comprising fatty acyl, sterol, glycerol-, glycerophopho-, sphingo-, and endocannabinoid-lipid metabolism. Very polar metabolites were not included in this analysis since we were focusing largely on synaptic junctions.

Due to the concatenated nature of our workflow, we were able to determine an exhaustive lipidome of the SJ fraction in not-yet-reported depth including lipid signaling molecules (PIPs, EC), membrane components (PC, PE, PS, PI), energy building blocks (TAG, STE) and compartment-specific lipids such as cardiolipins and gangliosides. This diverse lipid inventory underscores that the synaptic membrane is closely connected to mitochondria, ER, and lipid droplets needed to fuel the demands of a very high membrane exchange due to vesicle release. Surprisingly, almost 30% of all identified lipids were sphingolipids (Table S6). Besides commonly found Cer and SM carrying the long chain bases (LCBs) 18:0;2 and 18:1:2, we also identified the recently described LCB 18:2:2 (Karsai et al., 2020) across almost all sphingolipids. As compared to other LCB, LCB 18:2:2 is somehow special since LCBs usually contain a single Δ4E double bond (mostly d18:1), whereas the dienic LCB sphingadienine (d18:2) contains a second double bond at the Δ14Z position, which is likely to impact microdomain formation and indicates the presence of an active de-toxification pathway for the neurotoxic atypical cytotoxic 1-deoxysphinganine (Alecu et al., 2017). Based on this quantitative inventory, mathematical modeling of synaptic membrane fluidity, fission, and fusion processes will become easier and more precise, mass action calculation of lipid synthesis and signaling pathways can use the provided lipid concentration and metabolic network to steer the development of synapse-specific lipid signaling/metabolic models, and GO-terms such as those provided by the SynGO consortium (Koopmans et al., 2019) can be enriched with the provided information of this lipid inventory.

To underscore the heuristic value of the multiomics workflow for the generation of novel hypotheses, we compared the lipidome and proteome from the same synaptic junction sample from mice raised in EE or SE. We chose environmental stimulation to test whether this approach is suitable to uncover lipid metabolic pathways that are altered by physiological interventions relevant for cognition. It should be stressed that we only followed up on one hypothesis and that other interesting and testable hypotheses might be delineated from the dataset (accessible under PXD017997, MTBLS1531). Thus, evaluation of the data under different aspects of altered protein interactions in other networks might yield further insights. For instance, the levels of changing NADH-ubiquinone oxidoreductases likely indicate a regulation of the lipid category of prenol lipids so far not investigated, which however is highly important for energy transfer at the synaptic junction. In addition, high abundant short chain ceramides such as Cer 18:0;2/16:0, Cer 18:0;2/18:0, and their corresponding long chain base 18:1 and 18:2 derivatives (Table S1F) are dramatically increased in synaptic junctions as seen in the inventory study. At this point, we can only speculate about their impact, but an increase of abundant ceramide species was shown to enlarge the diameters of ceramide-rich platforms (CRP) (Burgert et al., 2017), and combined with a decreased length of these ceramides, this could change the solubility of proteins in such domains (Bock and Gulbins, 2003) and thus influence partitioning of proteins and signaling at the junction. Surprisingly, we also observed a cholesterol phospholipid ratio shift to 1:4, a shift that has the potential to increase membrane fluidity and lateral pressure. Membrane fluidity is strongly

Figure 6. LTP induction in acute slices from mice raised in EE and postsynaptic localization of ABHD6 and FAAH is regulated by CB1R signaling

(A–C) Involvement of CB1 receptors in LTP formation induced by repeated theta-burst stimulation (TBS) sequences in SE and EE mice. Induction of LTP by 8 repeats of a TBS sequence that consisted of 10 bursts of 5 stimuli every 30 s resulted in a stable potentiation under control condition (DMSO). However, application of the CB1R antagonist rimonabant (1 μM) over the whole recording period resulted in a declined potentiation in SE mice (C). Data are presented as mean ± SEM. $^{**}p \leq 0.01$, $^{*}p \leq 0.05$.

(D–G) Cells were transfected with MARCKS-GFP on DIV 15 and fixed on DIV 16. (D) Immunofluorescence staining of Shank3, Synaptopodin and ABHD6. Individual spines immunopositive (1,2) or immunonegative for ABHD6 (3) are shown. STED-imaging of Synapopodin reveals prominent co-localization of ABHD6 in Shank3 positive spines (E). Quantification of colocalization of ABHD6 and Synaptopodin with Shank3 (F) and the colocalization of Synaptopodin and ABHD6 in Shank3 positive synapses (G) (n = 15 cells). Data are presented as boxplots with whiskers from minimum to maximum value, $^{**}p \leq 0.01$, $^{***}p \leq 0.001$, $^{****}p \leq 0.0001$

(H–O) Hippocampal neurons were silenced with 1 μM TTX for 48 h. (I–O) The cells were fixed and stained with antibodies directed against MAP2, Shank3 and ABHD6 or FAAH at DIV 21. Immunofluorescence of ABHD6 (n = 28 cells) (I) and FAAH (n = 9 cells) (N) was analyzed in Shank3 labeled synapses. (I) and (N) Hippocampal neurons were treated for 48 h with the CB1 antagonist AM251 and cells fixed at DIV 21 were probed for MAP2, Shank3 and ABHD6 or FAAH immunoreactivity. Immunofluorescence intensity of ABHD6 (M) (n = 18 cells) and FAAH (O) (n = 23 cells) was quantified in Shank3 labeled synapses.

(P and Q) Staining with a Synaptopodin antibody after blockage of CB1R with AM251 reveals a displacement of the Synaptopodin-positive spine apparatus (n = 11 cells).

Data are presented as boxplots with whiskers from minimum to maximum value. Scale bars are 2.5 μm in (D), 2.5 μm in (E), 5 μm in (H), 5 μm in (J), 5 μm in (L), 5 μm in (N) and 5 μmin (P).

See also Figure S6 and S7.

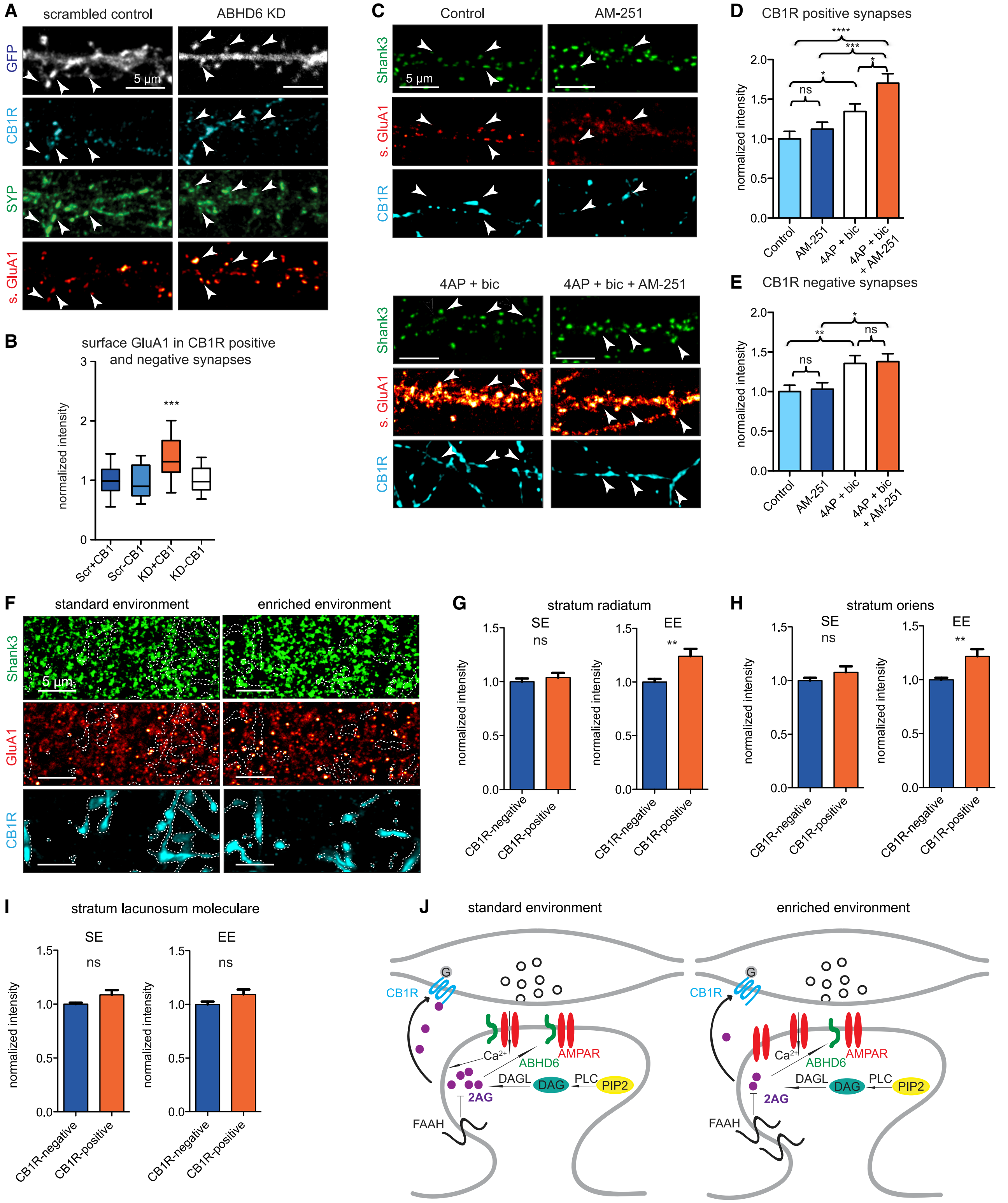

Figure 7. Regulation of GluA1 surface expression in CB1R positive synapses

(A and B) Hippocampal primary neurons were transfected with an ABHD6-knockdown or scrambled control construct at DIV 9 and live stained for GluA1 at DIV 14. Post-fixation the cells were stained with antibodies directed against synaptophysin and CB1. Scale bar is 5 µm. (A). Synaptic GluA1 levels were quantified in

(legend continued on next page)

influenced by cholesterol which is impeding acyl chain packing due to its inflexibility and therefore directly increases membrane rigidity (Goñi, 2014; Laude and Prior, 2012). These physical characteristics are shaping the underlying basis for curvature, thickness, and tension that influence cell signaling and microdomain formation (Sohn et al., 2018). Therefore, it is not surprising that higher cholesterol levels (e.g., induced by postsynaptic trafficking defects leads to impaired LTP with cognitive deficits [Mitroi et al., 2019]), whereas reduced cholesterol level can lead to mobilization of AMPARs (Brachet et al., 2015). It is tempting to speculate that this will ease lateral diffusion and exchange of transmembrane proteins. Finally, we also observed changes in some of the high abundant SM species. Sphingolipids are highly enriched in neuronal membranes. A fine balance between synthesis of sphingolipids and their degradation is required for normal brain homeostasis and function, since they function as plasma membrane lipids and signaling molecules (Allende et al., 2021).

Since ECS—to the best of our knowledge—has previously not been linked to the effects of EE on hippocampal function, we followed up on this dataset. Based on the multiomics workflow, we here propose a mechanism by which alterations in the postsynaptic association of ABHD6 and FAAH interact with reduced levels of 2-AG to facilitate an ECS-sensitive form of TBS-LTP at a subset of synapses (Figure 7J). In brief, we postulate that lower postsynaptic 2-AG levels, derived from increased hydrolase or decreased DAG activity negatively influence the postsynaptic localization of ABHD6, and this in turn, positively affects surface expression of GluA1 (Figure 7J). In this scenario, it is difficult to isolate the initial trigger for the observed changes, but it might be that generally elevated synaptic activity results in elevated postsynaptic FAAH levels and/or a retraction of the spine apparatus with concomitant removal of ABHD6. Of note, the association of the ER with spine synapses is dynamic and activity-dependent by itself (Perez-Alvarez et al., 2020).

The major degradative pathway of 2-AG is the hydrolysis to arachidonic acid and glycerol. MAGL is the major catabolic enzyme, but it is questionable whether the enzyme is indeed present in spines (see for instance Figures S7I and S7J). Most studies refer to a presynaptic localization and expression in astrocytes. Thus, although FAAH or ABHD6 are secondary in their net effect on 2-AG levels, the postsynaptic levels appear to control the synaptic localization of ABHD6 but not of FAAH. Since ABHD6 is at the same time an auxiliary of AMPAR that negatively regulates surface expression, synaptic displacement of ABHD6 is followed by an increase of GluA1 surface expression exclusively at CB1R positive synapses (Figure 7J). Although FAAH has a clearly dominant role in catabolism of anandamide, which is lower abundant in the hippocampus than 2-AG, it is also enzymatically active in the degradation of 2-AG under certain circumstances (Di Marzo and Maccarrone, 2008). AEA and 2-AG are considered the main endogenous mediators of cannabinoid signaling at synapses; however, it would be interesting to determine palmitoylethanolamide and oleoylethanolamide levels following EE, which are major substrates for FAAH and usually present at much higher concentration in tissues compared to anandamides. Moreover, ABHD12 is also known to be involved in 2-AG hydrolysis, but we could not observe a significant regulation of protein levels. Since ABHD12 is relatively low abundant in the hippocampus and is mainly expressed in microglia (Savinainen et al., 2012) we have not followed up on a possible synaptic function following EE.

Lower 2-AG levels will reduce CB1R signaling, and this reduction might then concomitantly reduce the postsynaptic expression of ABHD6 (Figure 7J), possibly by retraction of the ER. Taken together, this scenario provides a plausible explanation how ECS is linked to excitatory signaling at a subset of synapses in EE, and this link, in turn, might explain why in contrast to homecaged controls a weak-θ-burst protocol in EE mice is under negative control of CB1R signaling. In the latter case ABHD6 will likely relocate to CB1R-positive synapses, which then should result in reduced surface expression of GluA1. Our major aim was to showcase that testable hypothesis derived from the compartment-specific multiomics workflow introduced in this study and its analysis of lipid metabolism. However, studies in hippocampal primary neurons have certain limitations and further *in vivo* analysis linking changes in ECS in the brain of mice raised in EE to behavior is therefore ultimately warranted. Thus, although open questions remain, the experimental data point to a plausible scenario as to how EE might impact synaptic plasticity at a subset of CB1R-positive excitatory synapses.

STAR★METHODS

Detailed methods are provided in the online version of this paper and include the following:

- KEY RESOURCES TABLE
- RESOURCE AVAILABILITY
    - Lead contact
    - Materials availability
    - Data and code availability
- EXPERIMENTAL MODEL AND SUBJECT DETAILS
    - Rat Primary Hippocampal Culture

CB1 positive and negative synapses in control (n = 48 cells) and KD conditions (n = 48 cells) (B). In (B) data are presented as boxplots with whiskers from 10 to 90 percent. ***$p \leq 0.001$ (Student's t test).

(C–E) Surface expression of GluA1 was quantified in synapses positive for Shank3 and CB1R. Immunofluorescence staining of CB1R and Shank3 was done post-fixation. Cells at DIV 15 surface stained for GluA1 (Control (n = 32 cells); 10 μM Am251 (48 h) (n = 25 cells); 50 μM Bicuculline, 2 mM 4AP (30 min) (n = 32 cells), 50 μM Bicuculline, 2 mM 4AP (30 min) and 10 μM Am251 (48 h) (n = 29 cells). Scale bar is 5 μm.

(D) Synapses are depicted that are positive for Shank3 and negative for CB1R (E).

(F) Cryosections from 4 EE and 4 SE animals were stained for Shank3, GluA1 and CB1R. Scale bar is 5 μm.

(G–I) The intensity of the GluA1 staining was quantified in CB1R positive and CB1R negative synapses of the stratum radiatum (G), the stratum oriens (H) and stratum lacunosum moleculare (I). In (D)–(I), data are presented as mean + SEM. *$p \leq 0.05$ **$p \leq 0.01$ (Student's t test).

(J) Schematic of molecular dynamics in CB1R positive excitatory synapses in SE as compared to EE. See also Figure S7.

- METHOD DETAILS
    - ○ Materials and standards
    - ○ Enriched environment
    - ○ Subcellular fractionation
    - ○ Sample preparation for shotgun **lipidomics, endocannabinoid and sphingolipid** analysis
    - ○ Shotgun lipidomics
    - ○ Targeted sphingolipid analysis
    - ○ Targeted endocannabinoid analysis
    - ○ Sample preparation and phosphoinositide (PIP) analysis
    - ○ Sample preparation and ganglioside analysis
    - ○ Proteomics sample preparation
    - ○ Label free proteomics analysis
    - ○ Label free proteomics data analysis
    - ○ TMT-based proteomics data analysis
    - ○ Functional Annotation and Pathway Enrichment Analysis
    - ○ Transfections
    - ○ Treatments
    - ○ Immunocytochemistry
    - ○ Ultrastructural analysis with transmission electron microscopy
    - ○ Immunohistochemistry (IHC)
    - ○ Image acquisition
    - ○ Image analysis
    - ○ Immunoblotting and analysis
    - ○ Acute hippocampal slice preparation and electrophysiology
- QUANTIFICATION AND STATISTICAL ANALYSIS

SUPPLEMENTAL INFORMATION

Supplemental information can be found online at https://doi.org/10.1016/j.celrep.2021.109797.

ACKNOWLEDGMENTS

The authors gratefully acknowledge the professional technical assistance of C. Borutzki, S. Hochmuth, M. Marunde. We want to thank J. Bär, M. Andres-Alonso, and M. Sperveslage for preparing neuronal primary cultures. We also want to thank K. Mackie for the generous gift of the ABHD6 antibody. This study was supported by the Ministerium für Kultur und Wissenschaft des Landes Nordrhein-Westfalen; the Senatsverwaltung für Wirtschaft, Technologie und Forschung des Landes Berlin; the Bundesministerium für Bildung und Forschung (BMBF 'Energi' FKZ: 01GQ1421B to M.R.K.); The EU Joint Programme Neurodegenerative Disease Research project STAD to M.R.K.; the Leibniz Foundation Leibniz Pakt für Forschung SAW-2017-ISAS-2 awarded to M.R.K. and R.A.; and by grants from the Deutsche Forschungsgemeinschaft (Kr1879 10-1; FOR 2419 TP3; RTG 2413 TP4; CRC1436 A02, A04, and Z01 to M.R.K. and FOR 2419 RP2; Emmy Noether Programm; Excellence Strategy – EXC-2049–390688087 to M.M.). We received further support from BMBF in the German Network Bioinformatics Infrastructure (de.NBI) initiative grants No. 031L0108A and 031 A 534B. M.H. and M.C. acknowledge the support of grant project No. 21-20238S sponsored by the Czech Science Foundation. G.M.G. was supported by a Alexander-von-Humboldt Foundation / CAPES post-doctoral research fellowship (99999.001756/2014-01).

AUTHOR CONTRIBUTIONS

Designed experiments (R.A., M.R.K., M.M., T.B., and C.C.), performed experiments (M.B., M.M., C.C., C.H., P.W., H.S., T.L., M.C., Y.F.H.C., G.M.G., M.D., M.S., and M.C.), analyzed and interpreted data (M.B., M.M., C.C., C.H., P.W., H.S., T.L., M.C., Y.F.H.C., G.M.G., M.D., M.S., M.C., and M.R.K.), provided tools and reagents (M.H., M.C., and N.H.), developed the manuscript concept and wrote the paper (M.R.K. and R.A.), and funding acquisition (M.R.K., M.M., and R.A.).

DECLARATION OF INTERESTS

The authors declare no competing interests.

Received: November 18, 2020
Revised: April 12, 2021
Accepted: September 15, 2021
Published: October 5, 2021

REFERENCES

Alecu, I., Othman, A., Penno, A., Saied, E.M., Arenz, C., von Eckardstein, A., and Hornemann, T. (2017). Cytotoxic 1-deoxysphingolipids are metabolized by a cytochrome P450-dependent pathway. J. Lipid Res. *58*, 60–71.

Allende, M., L., Zhu, H., Kono, M., Hoachlander-Hobby, L., E., Huso, V., L., and Proia, R., L.. (2021). Genetic defects in the sphingolipid degradation pathway and their effects on microglia in neurodegenerative disease. Cell Signal *78*, 109879.

Almeida, R., Berzina, Z., Arnspang, E.C., Baumgart, J., Vogt, J., Nitsch, R., and Ejsing, C.S. (2015). Quantitative spatial analysis of the mouse brain lipidome by pressurized liquid extraction surface analysis. Anal. Chem. *87*, 1749–1756.

Anderson, G.R., Aoto, J., Tabuchi, K., Földy, C., Covy, J., Yee, A.X., Wu, D., Lee, S.J., Chen, L., Malenka, R.C., and Südhof, T.C. (2015). β-Neurexins Control Neural Circuits by Regulating Synaptic Endocannabinoid Signaling. Cell *162*, 593–606.

Antonny, B., Vanni, S., Shindou, H., and Ferreira, T. (2015). From zero to six double bonds: phospholipid unsaturation and organelle function. Trends Cell Biol. *25*, 427–436.

Augustin, S.M., and Lovinger, D.M. (2018). Functional Relevance of Endocannabinoid-Dependent Synaptic Plasticity in the Central Nervous System. ACS Chem. Neurosci. *9*, 2146–2161.

Bénard, G., Massa, F., Puente, N., Lourenço, J., Bellocchio, L., Soria-Gómez, E., Matias, I., Delamarre, A., Metna-Laurent, M., Cannich, A., et al. (2012). Mitochondrial CB_1 receptors regulate neuronal energy metabolism. Nat. Neurosci. *15*, 558–564.

Benfenati, F., Greengard, P., Brunner, J., and Bahler, M. (1989). Electrostatic and hydrophobic interactions of synapsin I and synapsin I fragments with phospholipid bilayers. J Cell Biol *108*, 1851–1862.

Biesemann, C., Grønborg, M., Luquet, E., Wichert, S.P., Bernard, V., Bungers, S.R., Cooper, B., Varoqueaux, F., Li, L., Byrne, J.A., et al. (2014). Proteomic screening of glutamatergic mouse brain synaptosomes isolated by fluorescence activated sorting. EMBO J. *33*, 157–170.

Bjornson, R.D., Carriero, N.J., Colangelo, C., Shifman, M., Cheung, K.H., Miller, P.L., and Williams, K. (2008). X!!Tandem, an improved method for running X!tandem in parallel on collections of commodity computers. J. Proteome Res. *7*, 293–299.

Bock, J., and Gulbins, E. (2003). The transmembranous domain of CD40 determines CD40 partitioning into lipid rafts. FEBS Lett. *534*, 169–174.

Brachet, A., Norwood, S., Brouwers, J.F., Palomer, E., Helms, J.B., Dotti, C.G., and Esteban, J.A. (2015). LTP-triggered cholesterol redistribution activates Cdc42 and drives AMPA receptor synaptic delivery. J. Cell Biol. *208*, 791–806.

Brügger, B., Erben, G., Sandhoff, R., Wieland, F.T., and Lehmann, W.D. (1997). Quantitative analysis of biological membrane lipids at the low picomole level by nano-electrospray ionization tandem mass spectrometry. Proc. Natl. Acad. Sci. USA *94*, 2339–2344.

Burgert, A., Schlegel, J., Bécam, J., Doose, S., Bieberich, E., Schubert-Unkmeir, A., and Sauer, M. (2017). Characterization of Plasma Membrane

Ceramides by Super-Resolution Microscopy. Angew. Chem. Int. Ed. Engl. *56*, 6131–6135.

Carlin, R.K., Grab, D.J., Cohen, R.S., and Siekevitz, P. (1980). Isolation and characterization of postsynaptic densities from various brain regions: enrichment of different types of postsynaptic densities. J. Cell Biol. *86*, 831–845.

Chernomordik, L.V., and Kozlov, M.M. (2003). Protein-lipid interplay in fusion and fission of biological membranes. Annu. Rev. Biochem. *72*, 175–207.

Cho, K.O., Hunt, C.A., and Kennedy, M.B. (1992). The rat brain postsynaptic density fraction contains a homolog of the Drosophila discs-large tumor suppressor protein. Neuron *9*, 929–942.

Choi, M., Chang, C.Y., Clough, T., Broudy, D., Killeen, T., MacLean, B., and Vitek, O. (2014). MSstats: an R package for statistical analysis of quantitative mass spectrometry-based proteomic experiments. Bioinformatics *30*, 2524–2526.

Coman, C., Solari, F.A., Hentschel, A., Sickmann, A., Zahedi, R.P., and Ahrends, R. (2016). Simultaneous Metabolite, Protein, Lipid Extraction (SIMPLEX): A Combinatorial Multimolecular Omics Approach for Systems Biology. Mol. Cell. Proteomics *15*, 1453–1466.

DeVries, G., H., Zetusky, W., J., Zmachinski, C., and Calabrese, V., P.. (1981). Lipid composition of axolemma-enriched fractions from human brains. J Lipid Res *22*, 208–216.

Di Marzo, V., and Maccarrone, M. (2008). FAAH and anandamide: is 2-AG really the odd one out? Trends Pharmacol. Sci. *29*, 229–233.

Dieterich, D.C., and Kreutz, M.R. (2016). Proteomics of the Synapse–A Quantitative Approach to Neuronal Plasticity. Mol. Cell. Proteomics *15*, 368–381.

Ekroos, K., Chernushevich, I.V., Simons, K., and Shevchenko, A. (2002). Quantitative profiling of phospholipids by multiple precursor ion scanning on a hybrid quadrupole time-of-flight mass spectrometer. Anal. Chem. *74*, 941–949.

Ellis, S.R., Paine, M.R.L., Eijkel, G.B., Pauling, J.K., Husen, P., Jervelund, M.W., Hermansson, M., Ejsing, C.S., and Heeren, R.M.A. (2018). Automated, parallel mass spectrometry imaging and structural identification of lipids. Nat. Methods *15*, 515–518.

Fitzner, D., Bader, J.M., Penkert, H., Bergner, C.G., Su, M., Weil, M.T., Surma, M.A., Mann, M., Klose, C., and Simons, M. (2020). Cell-Type- and Brain-Region-Resolved Mouse Brain Lipidome. Cell Rep. *32*, 108132.

Goñi, F.M. (2014). The basic structure and dynamics of cell membranes: an update of the Singer-Nicolson model. Biochim. Biophys. Acta *1838*, 1467–1476.

Gulyas, A.I., Cravatt, B.F., Bracey, M.H., Dinh, T.P., Piomelli, D., Boscia, F., and Freund, T.F. (2004). Segregation of two endocannabinoid-hydrolyzing enzymes into pre- and postsynaptic compartments in the rat hippocampus, cerebellum and amygdala. Eur. J. Neurosci. *20*, 441–458.

Han, X. (2002). Characterization and direct quantitation of ceramide molecular species from lipid extracts of biological samples by electrospray ionization tandem mass spectrometry. Anal. Biochem. *302*, 199–212.

Han, X. (2007). Neurolipidomics: challenges and developments. Front. Biosci. *12*, 2601–2615.

Heo, S., Diering, G.H., Na, C.H., Nirujogi, R.S., Bachman, J.L., Pandey, A., and Huganir, R.L. (2018). Identification of long-lived synaptic proteins by proteomic analysis of synaptosome protein turnover. Proc. Natl. Acad. Sci. USA *115*, E3827–E3836.

Herzog, R., Schwudke, D., Schuhmann, K., Sampaio, J.L., Bornstein, S.R., Schroeder, M., and Shevchenko, A. (2011). A novel informatics concept for high-throughput shotgun lipidomics based on the molecular fragmentation query language. Genome Biol. *12*, R8.

Jurado, S., Benoist, M., Lario, A., Knafo, S., Petrok, C.N., and Esteban, J.A. (2010). PTEN is recruited to the postsynaptic terminal for NMDA receptor-dependent long-term depression. EMBO J. *29*, 2827–2840.

Karsai, G., Lone, M., Kutalik, Z., Brenna, J.T., Li, H., Pan, D., von Eckardstein, A., and Hornemann, T. (2020). FADS3 is a Δ14Z sphingoid base desaturase that contributes to gender differences in the human plasma sphingolipidome. J. Biol. Chem. *295*, 1889–1897.

Katona, I., and Freund, T.F. (2012). Multiple functions of endocannabinoid signaling in the brain. Annu. Rev. Neurosci. *35*, 529–558.

Kononenko, N.L., and Haucke, V. (2015). Molecular mechanisms of presynaptic membrane retrieval and synaptic vesicle reformation. Neuron *85*, 484–496.

Koopmans, F., van Nierop, P., Andres-Alonso, M., Byrnes, A., Cijsouw, T., Coba, M.P., Cornelisse, L.N., Farrell, R.J., Goldschmidt, H.L., Howrigan, D.P., et al. (2019). SynGO: An Evidence-Based, Expert-Curated Knowledge Base for the Synapse. Neuron *103*, 217–234.e4.

Laude, A.J., and Prior, I.A. (2012). Europe PMC Funders Group Plasma membrane microdomains. organisation, function and trafficking *21*, 193–205.

Lauwers, E., Goodchild, R., and Verstreken, P. (2016). Membrane Lipids in Presynaptic Function and Disease. Neuron *90*, 11–25.

Lerner, R., Post, J.M., Ellis, S.R., Vos, D.R.N., Heeren, R.M.A., Lutz, B., and Bindila, L. (2018). Simultaneous lipidomic and transcriptomic profiling in mouse brain punches of acute epileptic seizure model compared to controls. J. Lipid Res. *59*, 283–297.

Lois, C., Hong, E.J., Pease, S., Brown, E.J., and Baltimore, D. (2002). Germline transmission and tissue-specific expression of transgenes delivered by lentiviral vectors. Science *295*, 868–872.

Marrs, W.R., Blankman, J.L., Horne, E.A., Thomazeau, A., Lin, Y.H., Coy, J., Bodor, A.L., Muccioli, G.G., Hu, S.S.J., Woodruff, G., et al. (2010). The serine hydrolase ABHD6 controls the accumulation and efficacy of 2-AG at cannabinoid receptors. Nat. Neurosci. *13*, 951–957.

Martin, M.G., Ahmed, T., Korovaichuk, A., Venero, C., Menchón, S.A., Salas, I., Munck, S., Herreras, O., Balschun, D., and Dotti, C.G. (2014). Constitutive hippocampal cholesterol loss underlies poor cognition in old rodents. EMBO Mol. Med. *6*, 902–917.

Mitroi, D.N., Pereyra-Gómez, G., Soto-Huelin, B., Senovilla, F., Kobayashi, T., Esteban, J.A., and Ledesma, M.D. (2019). NPC1 enables cholesterol mobilization during long-term potentiation that can be restored in Niemann-Pick disease type C by CYP46A1 activation. EMBO Rep. *20*, e48143.

Molenaar, M.R., Jeucken, A., Wassenaar, T.A., van de Lest, C.H.A., Brouwers, J.F., and Helms, J.B. (2019). LION/web: a web-based ontology enrichment tool for lipidomic data analysis. Gigascience *8*, 1–10.

Nagy, A., Baker, R., R., Morris, S., J., and Whittaker, V., P.. (1976). The preparation and characterization of synaptic vesicles of high purity. Brain Res *109*, 285–309.

Ohline, S.M., and Abraham, W.C. (2019). Environmental enrichment effects on synaptic and cellular physiology of hippocampal neurons. Neuropharmacology *145* (*Pt A*), 3–12.

Peng, B., Weintraub, S.T., Coman, C., Ponnaiyan, S., Sharma, R., Tews, B., Winter, D., and Ahrends, R. (2017). A Comprehensive High-Resolution Targeted Workflow for the Deep Profiling of Sphingolipids. Anal. Chem. *89*, 12480–12487.

Peng, B., Geue, S., Coman, C., Münzer, P., Kopczynski, D., Has, C., Hoffmann, N., Manke, M.C., Lang, F., Sickmann, A., et al. (2018). Identification of key lipids critical for platelet activation by comprehensive analysis of the platelet lipidome. Blood *132*, e1–e12.

Peng, B., Kopczynski, D., Pratt, B.S., Ejsing, C.S., Burla, B., Hermansson, M., Benke, P.I., Tan, S.H., Chan, M.Y., Torta, F., et al. (2020). LipidCreator workbench to probe the lipidomic landscape. Nat. Commun. *11*, 2057.

Perez-Alvarez, A., Yin, S., Schulze, C., Hammer, J.A.I., Wagner, W., and Oertner, T.G. (2020). Endoplasmic reticulum visits highly active spines and prevents runaway potentiation of synapses. Nat. Commun. *11*, 5083.

Piomelli, D., Astarita, G., and Rapaka, R. (2007). A neuroscientist's guide to lipidomics. Nat. Rev. Neurosci. *8*, 743–754.

Puchkov, D., and Haucke, V. (2013). Greasing the synaptic vesicle cycle by membrane lipids. Trends Cell Biol. *23*, 493–503.

Reichmann, F., Painsipp, E., Holzer, P., Kummer, D., Bock, E., and Leitinger, G. (2015). A novel unbiased counting method for the quantification of synapses in the mouse brain. J. Neurosci. Methods *240*, 13–21.

Rusten, T.E., and Stenmark, H. (2006). Analyzing phosphoinositides and their interacting proteins. Nat. Methods *3*, 251–258.

Savinainen, J., R., Saario, S., M., and Laitinen, J., T.. (2012). The serine hydrolases MAGL, ABHD6 and ABHD12 as guardians of 2-arachidonoylglycerol signalling through cannabinoid receptors. Acta Physiol (Oxf) *204* (*2*), 267–276.

Schindelin, J., Arganda-Carreras, I., Frise, E., Kaynig, V., Longair, M., Pietzsch, T., Preibisch, S., Rueden, C., Saalfeld, S., Schmid, B., et al. (2012). Fiji: an open-source platform for biological-image analysis. Nat. Methods *9*, 676–682.

Schuhmann, K., Almeida, R., Baumert, M., Herzog, R., Bornstein, S.R., and Shevchenko, A. (2012). Shotgun lipidomics on a LTQ Orbitrap mass spectrometer by successive switching between acquisition polarity modes. J. Mass Spectrom. *47*, 96–104.

Sohn, J., Lin, H., Fritch, M.R., and Tuan, R.S. (2018). Influence of cholesterol/caveolin-1/caveolae homeostasis on membrane properties and substrate adhesion characteristics of adult human mesenchymal stem cells. Stem Cell Res. Ther. *9*, 86.

Soni, S.P., LoCascio, D.S., Liu, Y., Williams, J.A., Bittman, R., Stillwell, W., and Wassall, S.R. (2008). Docosahexaenoic acid enhances segregation of lipids between raft and nonraft domains: 2H-NMR study. Biophys. J. *95*, 203–214.

Sud, M., Fahy, E., Cotter, D., Brown, A., Dennis, E.A., Glass, C.K., Merrill, A.H., Jr., Murphy, R.C., Raetz, C.R., Russell, D.W., and Subramaniam, S. (2007). LMSD: LIPID MAPS structure database. Nucleic Acids Res. *35*, D527–D532.

Takamori, S., Holt, M., Stenius, K., Lemke, E., A., Gronborg, M., Riedel, D., Urlaub, H., Schenck, S., Brugger, B., Ringler, P., et al. (2006). Molecular anatomy of a trafficking organelle. Cell *127*, 831–846.

Tsuriel, S., Geva, R., Zamorano, P., Dresbach, T., Boeckers, T., Gundelfinger, E.D., Garner, C.C., and Ziv, N.E. (2006). Local sharing as a predominant determinant of synaptic matrix molecular dynamics. PLoS Biol. *4*, e271.

Tulodziecka, K., Diaz-Rohrer, B.B., Farley, M.M., Chan, R.B., Di Paolo, G., Levental, K.R., Waxham, M.N., and Levental, I. (2016). Remodeling of the postsynaptic plasma membrane during neural development. Mol. Biol. Cell *27*, 3480–3489.

Walker, J., H., and Agoston, D., V.. (1987). The synaptic vesicle and the cytoskeleton. Biochem J *247*, 249–258.

Wei, M., Zhang, J., Jia, M., Yang, C., Pan, Y., Li, S., Luo, Y., Zheng, J., Ji, J., Chen, J., et al. (2016). α/β-Hydrolase domain-containing 6 (ABHD6) negatively regulates the surface delivery and synaptic function of AMPA receptors. Proc. Natl. Acad. Sci. USA *113*, e2695, e704.

Wendholt, D., Spilker, C., Schmitt, A., Dolnik, A., Smalla, K.H., Proepper, C., Bockmann, J., Sobue, K., Gundelfinger, E.D., Kreutz, M.R., and Boeckers, T.M. (2006). ProSAP-interacting protein 1 (ProSAPiP1), a novel protein of the postsynaptic density that links the spine-associated Rap-Gap (SPAR) to the scaffolding protein ProSAP2/Shank3. J. Biol. Chem. *281*, 13805–13816.

Yu, Q., He, Z., Zubkov, D., Huang, S., Kurochkin, I., Yang, X., Halene, T., Willmitzer, L., Giavalisco, P., Akbarian, S., and Khaitovich, P. (2020). Lipidome alterations in human prefrontal cortex during development, aging, and cognitive disorders. Mol. Psychiatry *25*, 2952–2969.

STAR★METHODS

KEY RESOURCES TABLE

REAGENT or RESOURCE	SOURCE	IDENTIFIER
Antibodies		
Rabbit anti ABHD6	Ken Mackie; Indiana University Bloomington	N/A
Guinea pig anti Shank3	Synaptic Systems	Cat#162304; RRID:AB_2619863 IHC 1:300 ICC 1:1000
Mouse anti MAP2	Sigma	Cat#M440;, RRID:AB_477193 IHC 1:500
Guinea pig anti MAP2	Synaptic Systems	Cat# 188 004; RRID:AB_2138181 IHC 1:500
Guinea pig anti Bassoon	Synaptic Systems	Cat#141004; RRID:AB_2290619 IHC 1:500
Mouse anti Gephyrin	Synaptic systems	Cat#147011; RRID:AB_887719 IHC 1:500
Mouse anti PSD 95	UC Davis/NIH, NeuroMab	Cat#75-028; RRID:AB_2307331 WB 1:1000
Mouse anti CB1R	Synaptic Systems	Cat# 258 003; RRID:AB_2619970 CB1-R IHC, ICC 1:500
Rabbit anti GluA1	Merck Millipore	Cat#ABN241; RRID:AB_2721164 Surface staining 1:500
Rabbit anti GluA1	Cell Signaling Technology	Cat#D4N9V; RRID:AB_2732897 IHC 1:500
Rabbit anti FAAH	Cayman Chemicals	Cat#101600; RRID:AB_10078701 ICC, IHC 1:200
Mouse anti FAAH	Abcam	Cat#ab54615; RRID:AB_2101890 WB 1:1000
Rabbit anti MAGL	Abcam	Cat#ab24701; RRID:AB_448238 ICC:1:500
Mouse anti Synaptophysin1	Synaptic Systems	Cat#101 011; RRID:AB_887824 ICC, IHC 1:500
Mouse anti beta Tubulin	Sigma-Aldrich	Cat#T8660; RRID:AB_477590 WB 1:1000
Mouse anti Synaptopodin	Origene	Cat#BM5086; RRID:AB_1007636 Clone G1D4
Anti-mouse-AlexaFluor 488	ThermoFisher Scientific	Cat#A-11001, RRID:AB 2534069, IF- 1:500
Anti-guinea pig-AlexaFluor 488	ThermoFisher Scientific	Cat#A-11073; RRID:AB_2534117 IF- 1:500
Anti-mouse-AlexaFluor 568	ThermoFisher Scientific	Cat#A-11004; RRID:AB_2534072 IF- 1:500
Anti-Rabbit IgG–Abberior STAR 635P	Abberior	Cat#2-0012-007-2 IHC/ICC 1:500
Anti-guinea pig-AlexaFluor 568	ThermoFisher Scientific	Cat#A-11075; RRID:AB_2534119 IF- 1:500
Anti-rabbit-IgG-HRP	Dianova	Cat#111-035-144; RRID:AB_2307391 1:20000
Anti-mouse-IgG-HRP	Dianova	Cat#115-035-146; RRID:AB_2307392 1:20000
GFP-Booster Atto488	Nanotag	Cat#N0304-At488-L; RRID:AB_2744627 IF-1:250
RFP-Booster Atto580	Nanotag	Cat#N0401-Ab580-L; RRID:AB_2744601 IF-1:250
Anti-rabbit-ATTO 647N	Sigma	Cat#40839; RRID:AB_1137669 IF 1:250

(*Continued on next page*)

Continued

REAGENT or RESOURCE	SOURCE	IDENTIFIER
AbberiorStar 580 guinea pig	Abberior	Cat#2-0012-005-7; RRID:AB_2810981 1:250
AbberiorStar 580 mouse	Abberior	Cat#2-0012-005-1; RRID:AB_2810981 1:250
Bacterial strains		
E.coli XL10Gold	Agilent	Cat#200314
Chemicals, peptides, and recombinant proteins		
Formic acid	Biosolve	Cat#6914143
Tert-butyl methyl ether (MTBE)	Sigma Aldrich	Cat#650560-1L
HPLC-grade phosphoric acid (85-90%)	Sigma Aldrich	Cat#79617-250ML
Glucose	Sigma Aldrich	Cat#G5767-500G
Chloroform	Sigma Aldrich	Cat#650498-1L
Acetonitrile ULC/MS-grade solvents	Biosolve	Cat#1204102
Methanol ULC/MS-grade solvents	Biosolve	Cat#13684102
1-butanol	Sigma Aldrich	Cat#360465-500ML
Isopropanol	Sigma Aldrich	Cat#1010402500
1-heptadecanoyl-2-(9Z-tetradecenoyl)-sn-glycero-3-phosphate (PA 17:0/14:1)	Avanti	Cat#LM-1404
1-heptadecanoyl-2-(5Z,8Z,11Z,14Z-eicosatetraenoyl)-sn-glycero-3-phosphocholine (PC 17:0/20:4)	Avanti	Cat#LM-1002
1-nonadecanoyl-2-hydroxy-sn-glycero-3-phosphocholine (LPC 19:0)	Avanti	Cat#855776
1-heneicosanoyl-2-(4Z,7Z,10Z,13Z,16Z,19Z-docosahexaenoyl)-sn-glycero-3-phosphoethanolamine (PE 21:0/22:6)	Avanti	Cat#LM-1103
1-heptadecanoyl-2-(5Z,8Z,11Z,14Z-eicosatetraenoyl)-sn-glycero-3-phospho-(1’-rac-glycerol) (PG 17:0/20:4)	Avanti	Cat#LM-1202
1-heneicosanoyl-2-(4Z,7Z,10Z,13Z,16Z,19Z-docosahexaenoyl)-sn-glycero-3-phospho-(1’-myo-inositol) (PI 21:0/22:6)	Avanti	Cat#LM-1503
1-heptadecanoyl-2-(5Z,8Z,11Z,14Z-eicosatetraenoyl)-sn-glycero-3-phospho-L-serine (PS 17:0/20:4)	Avanti	Cat#LM-1302
1’,3′-bis[1,2-dioleoyl-sn-glycero-3-phospho]-sn-glycerol (CL 18:1/18:1/18:1/18:1)	Avanti	Cat#710335
1,2-didecanoyl-sn-glycerol (DAG 10:0/10:0)	Avanti	Cat#800810
Cholest-5-en-3β-yl heptadecanoate (ChoE 17:0)	Avanti	Cat#110864
Cholesterol-d7 (D7-Chol)	Avanti	Cat#700041
Lyso Sphingomyelin d17:1 (SPC)	Avanti	Cat#LM-2320
C12 Mono-Sulfo Galactosyl(β) Ceramide (HexCerS d18:1/12:0)	Avanti	Cat#860573
SPLASH Lipidomics Mass Spec Standard	Avanti	Cat#330707
Ceramide/Sphingoid internal standard mixture II	Avanti	Cat#LM 6005
1-heptadecanoyl-2-arachidonoyl-sn-glycero-3-phospho-1’-myo-inositol-3′-phosphate (PI3P 17:0/20:4)	Avanti	Cat#LM1900
1,2-dioleoyl-sn-glycero-3-phospho-1-myo-inositol-3′,4’-bisphosphate (PI(3,4)P2 18:1/18:1)	Avanti	Cat#850153
1,2-dioleoyl-sn-glycero-3-phospho-1’-myo-inositol-4’,5′-bisphosphate (PI(4,5)P2 18:1/18:1)	Avanti	Cat#850155
1,2-dioleoyl-sn-glycero-3-phospho-1’-myo-inositol-3′,5′-bisphosphate (PI(3,5)P2 18:1/18:1)	Avanti	Cat#850154
1-heptadecanoyl-2-arachidonoyl-sn-glycero-3-phospho-1’-myo-inositol-3′-triphosphate (PI(3,4,5)P3 17:0/20:4)	Avanti	Cat#LM 1906
Cardiolipin Mix I	Avanti	Cat#LM 6003

(*Continued on next page*)

Continued

REAGENT or RESOURCE	SOURCE	IDENTIFIER
C18:0 GM3-d5	Avanti	Cat#860073
GM3 18:1,1/12:0 and GM1 18:1,1/12:0	Generated	0001, 0002
1,2,3-tritetradecanoylglycerol (TAG 14:0/14:0/14:0)	Sigma Aldrich	Cat#T5141
1,2-dipalmitoyl-glycero-phosphoinositol 4,5-biphosphate (PIP(4,5)-FP 16:0/16:0)	Echelon Biosciences	N/A
Stearoyl ethanolamide-d3	Cayman Chemical	Cat#14726
Oleoyl ethanolamide-d4	Cayman Chemical	Cat#9000552
Linoleoyl ethanolamine-d4	Cayman Chemical	Cat#9000553
Oleoyl Serotonin-d17	Cayman Chemical	Cat#9000694
2-arachidonoyl glycerol-d8	Cayman Chemical	Cat#362160
N-dodecanoylglycine-d23	Santa Cruz Biotechnology.	Cat#sc-477205
Palmitoyl ethanolamide-d4	Cayman Chemical	Cat#9000551
2-Arachidonoyl glycerol-d5	Cayman Chemical	Cat#362162
Arachidonoyl ethanolamide-d4	Cayman Chemical	Cat#10011178
Eicosapentaenoyl ethanolamide-d4	Cayman Chemical	Cat#9001835
Palmitoyl ethanolamide-d4	Cayman Chemical	Cat#10007824
Docosahexaenoyl ethanolamide	Sigma Aldrich	Cat#SML0563-5MG
Stearoyl ethanolamide	TCR	Cat#S686608
1-Monoolein	Larodan	Cat#3443-84-3
2-Monodocosahexaenoin	Larodan	Cat#31-2206-7
1-Monostearin	Larodan	Cat#31-1802-0
Anandamide (Arachidonyl ethanolamid	Cayman Chemical	Cat#10007270
N-stearyl Taurine	Cayman Chemical	Cat#10005610
N-Oleoyl Taurine	Cayman Chemical	Cat#10005609
N-Docosahexaenoyl Dopamine	Cayman Chemical	Cat#9001394
Docosahexaenoyl Serotonin	Cayman Chemical	Cat#9000639
Stearoyl Serotonin	Cayman Chemical	Cat#9000631
Oleoyl Serotonin	Cayman Chemical	Cat#9000629
Palmitoyl Ethanolamide	Cayman Chemical	Cat#90350
N-Oleoyl Valine	Cayman Chemical	Cat#90265
Eicosatrienoic Acid Ethanolamide	Cayman Chemical	Cat#90195
Linoleoyl Ethanolamide	Cayman Chemical	Cat#90155
2-Arachidonoyl Glycerol	Cayman Chemical	Cat#62160
N-Oleoyl Alanine	Cayman Chemical	Cat#20368
Oleoyl Ethanolamide	Cayman Chemical	Cat#20065
1-Palmitoyl Glycerol	Cayman Chemical	Cat#17882
N-Oleoyl-L-Serine	Cayman Chemical	Cat#13058
N-Oleoyl Dopamine	Cayman Chemical	Cat#10115
TMT10plex Isobaric Label Reagent Set	Thermo Fischer Scientific	Cat#90406
Lipofectamine 2000	Invitrogen	Cat#11668027
DMEM	GIBCO	Cat#41960-029
BrainPhys	StemCell	Cat#05790
Paraformaldehyde	Carl Roth	Cat#P087.5
Mowiol	Carl Roth	Cat#4-88
Triton X-100	Carl Roth	Cat#3051.3
B27	GIBCO	Cat#17504-044
Tetrodotoxin citrate (TTX)	Alomone labs	Cat# T-550
Bicuculline	Tocris Bioscience	Cat#2503
Am251	Cayman Chemicals	Cat#71670

(*Continued on next page*)

Continued

REAGENT or RESOURCE	SOURCE	IDENTIFIER
Rimonabant	Sigma	Cat# SML0800
D-AP5	Tocris Bioscience	Cat#0106
CNQX	Tocris Bioscience	Cat#0190
Deposited Data		
Lipidomic datasets of cells and tissue analyzed	This paper	Table S5
Lipidomics datasets at Metabolights: https://www.ebi.ac.uk/metabolights/MTBLS1531	Metabolights	MTBLS1531
PRIDE partner repository with the dataset identifier PXD017997	Pride	PXD017997
Experimental Models: Cell Lines		
Primary rat hippocampal cultures	UKE VTH	RjHan:WI
Experimental Models: Organisms/Strains		
Mice C57BL/6J	Charles River	N/A
Rat Wistar	Janvier	RjHan:WI
Oligonucleotides		
ABHD6 KD template: GCT ACT GAC TGA GAA GAG AAA (TCAAGAG) TTT CTC TTC TCA GTC AGTAGC	Intergrated DNA Technologies	N/A
FAAH KD template: GCC CAG ATG GAA CAC TAC AAA (TCAAGAG) TTT GTA GTG TTC CAT CTG GGC	Intergrated DNA Technologies	N/A
Scrambled control template: CTT CGC GCC GTA GTC TTA (TCAAGAG) TAA GAC TAC GGC GCG AAG	Intergrated DNA Technologies	N/A
Recombinant DNA		
EGFP N1	Clontech	Cat#6085-1
MARCKS-GFP	(Lois et al., 2002)	Addgene FUGW Plasmid # 14883
PSI-HIV-H1 (shRNA cloning vector)	System Biosciences	Cat#SI500A-1
Software and Algorithms		
Proteome Discoverer (version 2)	Thermo Scientific	https://www.thermofisher.com/at/en/home/industrial/mass-spectrometry/liquid-chromatography-mass-spectrometry-lc-ms/lc-ms-software/multi-omics-data-analysis/proteome-discoverer-software.html
Cytoscape (version 3.6.1)	Cytoscape Consortium	https://cytoscape.org/
Progenesis QI software version 4.1	Waters	https://www.nonlinear.com/progenesis/qi/
searchGui 1.14.4	CompOmicsTeam	http://compomics.github.io/projects/searchgui
PeptideShaker (version 1.04+)	CompOmicsTeam	http://compomics.github.io/projects/peptide-shaker
Mascot (version 2.4)	Matrixscience	http://www.matrixscience.com/mascot_support.html
X!Tandem (version 2015.12.15.2)	(Bjornson et al., 2008)	https://www.thegpm.org/TANDEM/
SynGo 1.0	SynGo consortium	https://syngoportal.org/index.html
LipidCreator (v1.1.0.736)	LIFS	https://lifs.isas.de/
LipidXplorer (v1.2.8.1)	LIFS	https://lifs.isas.de/
MSStats (Version 3.10.4)	(Choi et al., 2014)	https://www.bioconductor.org/packages/release/bioc/html/MSstats.html
OpenView Version 1.5	(Tsuriel et al., 2006)	N/A. Software available upon request from the authors
Fiji	(Schindelin et al., 2012)	https://fiji.sc/ RRID:SCR_002285
GraphPad Prism 8	GraphPad	https://www.graphpad.com/scientificsoftware/prism/

(*Continued on next page*)

Continued

REAGENT or RESOURCE	SOURCE	IDENTIFIER
Other		
UltiMate 3000-system	Thermo Fisher Scientific	N/A
Ultimate 3000 RSLC	Thermo Fisher Scientific	N/A
Agilent 1290 Infinity series	Agilent	N/A
Dionex ICS-5000 instrument	Thermo Fisher Scientific	N/A
TriVersa NanoMate ion source	Advion Biosciences	N/A
Q Exactive HF or Plus mass spectrometer	Thermo Fisher Scientific	N/A
Xevo G2-XS QTOF	Waters	N/A
QTRAP 6500	Applied Biosystems	N/A
TSQ Vantage	Thermo Fisher Scientific	N/A
Orbitrap Lumos Fusion	Thermo Fisher Scientific	N/A
Dionex IonPac AS11-HC column (250 mm × 2 mm, 4 μm particle size)	Thermo Fischer Scientific	Cat#052960
Ascentis Express C18 main column (150 mm × 2.1 mm, 2.7 μm)	Sigma Aldrich	Cat#53829-U
Ascentis Si column (150 mm x 2.1 mm, 3 μm particle size)	Sigma-Aldrich	Cat#581502-U
Sep-Pak C18 SPE cartridges	Waters	Cat#186006325
Acclaim C18 PepMap trap column (2 cm x 75 μm, 3 μm, 100 Å)	Thermo Fischer Scientific	Cat#164564-CMD
Acclaim C18 PepMap main column (15 cm x 75 μm, 3 μm, 100 Å)	Thermo Fischer Scientific	Cat#164568

RESOURCE AVAILABILITY

Lead contact

Further information and requests for resources and reagents should be directed to and will be fulfilled by the Lead Contact, Michael R. Kreutz (michael.kreutz@zmnh.uni-hamburg.de).

Materials availability

This study did not generate new unique reagents.

Data and code availability

Proteomics and lipidomics data on heavy membrane, synaptosome, and synaptic junction are provided in Table S1.

The mass spectrometry proteomics data have been deposited to the ProteomeXchange Consortium via the PRIDE partner repository with the dataset identifier: PXD017997.

Lipidomics raw data are available from Metabolights: https://www.ebi.ac.uk/metabolights/MTBLS1531 and are publicly available as of the date of publication.

This paper does not report original code.

Any additional information required to reanalyze the data reported in this paper is available from the lead contact upon request.

EXPERIMENTAL MODEL AND SUBJECT DETAILS

Animals were maintained in the animal facility of the Leibniz Institute for Neurobiology, Magdeburg (Germany) or ZMNH, Hamburg (Germany) under controlled environmental conditions. All animal experimentation was performed in accordance with the ARRIVE guidelines for animal experimentation, EU regulations and approved by the local ethical committee. For preparation of synaptic fractions, male rats (Han-Wistar) aged 10-11 weeks, were used. Male wild-type C57BL/6J mice (Charles River, country) were used. The mice were 4 weeks old on arrival. The mice were 5 weeks old at the start of the experiment and 11 weeks old at the end of the experiment.

Rat Primary Hippocampal Culture

Primary rat hippocampal cultures were prepared from Wistar rats (E18). The rats were decapitated, and the hippocampi were dissected. After treatment with trypsin at 37°C for 15 min and subsequent mechanical dissociation, cells were plated on 18 mm glass coverslips coated with poly-D-lysine at a density of 10.000 - 30.000 cells per well in DMEM medium (GIBCO) supplemented with 10% fetal bovine serum (FBS), 0.5 mM Glutamax (GIBCO). After 1 h media was exchanged to BrainPhysTM (GIBCO) neuronal medium supplemented with 1X SM1 (Stemcell), 0.5 mM glutamine (GIBCO). Cells were kept at 37°C, 5% CO_2 and 95% humidity until use.

METHOD DETAILS

Materials and standards

Formic acid, tert-butyl methyl ether (MTBE), ammonium formate (AF), ammonium acetate, acetic acid (HAc), potassium hydroxide (KOH), sodium hydroxide (NaOH), HPLC-grade phosphoric acid (85%–90%), sodium chloride, sodium bicarbonate, potassium chloride, glucose, chloroform, methylamine, HEPES and calcium chloride were purchased from Sigma Aldrich (Steinheim, Germany). The ULC/MS-grade solvents, acetonitrile (ACN), methanol (MeOH) were obtained from Biosolve (Valkenswaard, Netherlands) and 1-butanol and isopropanol (IPA) were purchased from Merck (Darmstadt, Germany). All solutions were prepared with ultrapure water (18 MΩ cm at 25°C). Sodium dodecyl sulfate (SDS) was obtained from Roth (Karlsruhe, Germany), tris(hydroxymethyl)-aminomethane (Tris) from Applichem (Darmstadt, Germany), and sodium chloride (NaCl) from Merck (Darmstadt, Germany). Lipids standards were purchased from Avanti (Alabaster, AL, USA) if not otherwise indicated, 1-heptadecanoyl-2-(9Z-tetradecenoyl)-sn-glycero-3-phosphate (PA 17:0/14:1, LM-1404), 1-heptadecanoyl-2-(5Z,8Z,11Z,14Z-eicosatetraenoyl)-sn-glycero-3-phosphocholine (PC 17:0/20:4, LM-1002), 1-nonadecanoyl-2-hydroxy-sn-glycero-3-phosphocholine (LPC 19:0, 855776), 1-heneicosanoyl-2-(4Z,7Z,10Z,13Z,16Z,19Z-docosahexaenoyl)-sn-glycero-3-phosphoethanolamine (PE 21:0/22:6, LM-1103), 1-heptadecanoyl-2-(5Z,8Z,11Z,14Z-eicosatetraenoyl)-sn-glycero-3-phospho-(1’-rac-glycerol) (PG 17:0/20:4, LM-1202), 1-heneicosanoyl-2-(4Z,7Z,10Z,13Z,16Z,19Z-docosahexaenoyl)-sn-glycero-3-phospho-(1’-myo-inositol) (PI 21:0/22:6, LM-1503), 1-heptadecanoyl-2-(5Z,8Z,11Z,14Z-eicosatetraenoyl)-sn-glycero-3-phospho-L-serine (PS 17:0/20:4, LM-1302), 1’,3′-bis[1,2-dioleoyl-sn-glycero-3-phospho]-sn-glycerol (CL 18:1/18:1/18:1/18:1, 710335), 1,2-didecanoyl-sn-glycerol (DAG 10:0/10:0, 800810), cholest-5-en-3β-yl heptadecanoate (ChoE 17:0, 110864), cholesterol-d7 (D7-Chol, 700041), lyso Sphingomyelin d17:1 (SPC, LM-2320), C12 Mono-Sulfo Galactosyl(β) Ceramide (HexCerS d18:1/12:0, 860573), SPLASH Lipidomics Mass Spec Standard (330707), Ceramide/Sphingoid internal standard mixture II (CerMix, LM 6005), 1-heptadecanoyl-2-arachidonoyl-sn-glycero-3-phospho-1’-myo-inositol-3′-phosphate (PI3P 17:0/20:4), 1,2-dioleoyl-sn-glycero-3-phospho-1-myo-inositol-3′,4’-bisphosphate (PI(3,4)P2 18:1/18:1, 850153), 1,2-dioleoyl-sn-glycero-3-phospho-1’-myo-inositol-4’,5′-bisphosphate (PI(4,5)P2 18:1/18:1, 850155), 1,2-dioleoyl-sn-glycero-3-phospho-1’-myo-inositol-3′,5′-bisphosphate (PI(3,5)P2 18:1/18:1, 850154) and 1-heptadecanoyl-2-arachidonoyl-sn-glycero-3-phospho-1’-myo-inositol-3′-triphosphate (PI(3,4,5)P3 17:0/20:4, LM 1906), Cardiolipin Mix I (LM 6003), C18:0 GM3-d5 (860073). The GM3 18:1,1/12:0 and GM1 18:1,1/12:0 were generated. 1,2,3-tritetradecanoylglycerol (TAG 14:0/14:0/14:0, T5141) was purchased from Sigma Aldrich (Steinheim, Germany) and 1,2-dipalmitoyl-glycerophosphoinositol 4,5-biphosphate (PIP(4,5)-FP 16:0/16:0) from Echelon Biosciences (Salt Lake City, UT) and N-dodecanoylglycine-d23 (sc-477205) from Santa Cruz Biotechnology. Stearoyl Ethanolamide-d3 (14726), N-oleoylethanolamide-d4 (9000552), linoleoyl ethanolamine-d4 (9000553, 9001841), 2-arachidonoyl glycerol-d5 (362162), 2-arachidonoyl glycerol-d8 (362160), arachidonoyl ethanolamide-d4 (10011178), eicosapentaenoyl ethanolamide-d4 (9001835), oleoyl serotonin-d17 (9000694), palmitoyl ethanolamide-d4 (10007824, 9000551), and α-linolenoyl ethanolamide-d4 (9001841) were purchased from Cayman Chemical (USA). N-dodecanoylglycine-d23. External standards such as Docosahexaenoyl ethanolamide was ordered from Sigma Aldrich (SML0563-5MG), stearoyl ethanolamide (S686608) from Toronto Chemical Research and 1 - monoolein (3443-84-3), 2 - monodocosahexaenoin (31-2206-7), 1 - monostearin (31-1802-0) from Larodan all other ESTDs were order form Cayman Chemicals including anandamide (10007270), N-stearyl taurine (10005610), N-oleoyl taurine (10005609), N - docosahexaenoyl dopamine (9001394), docosahexaenoyl serotonin (9000639), stearoyl serotonin (9000631), oleoyl serotonin (9000629), palmitoyl ethanolamide (90350), N-oleoyl valine (90265), eicosatrienoic acid ethanolamide (90195), linoleoyl ethanolamide (90155), 2 - arachidonoyl glycerol (62160), N-oleoyl alanine (20368), oleoyl ethanolamide (20065), 1-palmitoyl glycerol (17882), N-oleoyl-L-serine (13058), N-oleoyl dopamine (10115).

Enriched environment

A total of 168 male C57BL/6J mice (Charles River, country), 4 weeks old were used. Upon arrival, the animals were housed in a light-dark cycle of 12 h (lights on at 7:00 am) (4 per cage) with free access to food and water. After one week of adaption period to the experimental room, the animals were randomly assigned to either control or enriched environment (EE) group. To cover the most important aspects of EE, each cage (60 cm x 35 cm x 20 cm) had one running wheel, plastic house cups, acrylic tubes, bedding material (Nestlets, Ancare), and other objects with different textures and sizes, made of plastic, wood, rope, and glass. The cage also had a rope or wooden bridge attached to the grid, providing a fully three-dimensional exploration space. The control group cage consisted of a regular IVC cage. Animals were assigned either to EE or the control group and kept in these conditions for 6 weeks. Cages and objects were cleaned once a week. At the end of this period, the animals were euthanized, and the hippocampi were dissected for immediate synaptic junction preparation.

Subcellular fractionation

Preparation of synaptosomes and synaptic junctions was done as described previously (Carlin et al., 1980; Cho et al., 1992; Wendholt et al., 2006) with some minor modifications. In brief, hippocampi were homogenized in 10 ml/g buffer A (0.32 M sucrose, 5 mM HEPES, pH 7.4) including protease inhibitor cocktail (PI) and Phosphatase Inhibitor (PhosSTOP) and centrifuged at 1 000 g for

10 min. The pellet was re-homogenized and centrifuged in buffer A. The resulting pellet 1 containing nuclei and cell debris was discarded and the supernatants were combined. The combined supernatants were centrifuged at 12 000 g for 20 min and the supernatant (S2) was collected (Sorvall RC6, F13-14 × 50cy rotor). The pellet P2 was re-homogenized in buffer A and centrifuged as previously at 12 000 g for 20 min. The supernatant (S2′) was collected and combined with supernatant S2. The resulting pellet was collected as crude membrane fraction P2. One-eighth of the P2 fraction was collected and washed in PBS and centrifuged at 12 000 g for 20 min (Sorval RC6, F13-14xcy-rotor). Pellets were taken up in PBS, snap-frozen in liquid nitrogen and stored at −80°C. For further purification, the remaining P2-fraction was re-homogenized in buffer B (0.32 M sucrose, 5 mM Tris/HCl, PH 8.1). The homogenate was loaded on a 0.85 M/1.0 M/1.2 M sucrose step gradient and centrifuged at 85 000 g for 2 h (Beckmann XPN-80 centrifuge, SW32 Ti rotor). The synaptosomes were collected from the 1.0 M/1.2 M sucrose interphase. 40 percent of the solution was washed in PBS with PI and PhosSTOP and centrifuged at 90 000 g for 1 h (Beckmann XPN-80, SW32 Ti rotor). The pellets were resuspended and centrifuged at 90 000 g for 1h (TLA-55). Next, the pellets were frozen in liquid nitrogen and stored at −80°C. To isolate the synaptic junctions, the synaptosomes were opened by hypoosmotic shock. Hence, the synaptosomes were mixed for 30 min at 4°C in 1mM Tris/HCL pH 8.1 with PI and PhosSTOP. The samples were then centrifuged at 3 200 g for 30 min (Sorvall RC6, SS-34 rotor). The Pellet P3 was resuspended in 1.5 ml/g 5 mM Tris/HCl pH 8.1 with PI and PhosSTOP and loaded on a 1.0 M/1.2 M sucrose step gradient and centrifuged at 85 000 g for 2 h (Beckmann XPN-80 centrifuge, SW32 Ti rotor). The synaptic junctions were collected from the 1.0 M/1.2 M sucrose interphase and stored on ice overnight. They were resuspended in 10 mM phosphate buffered saline (PBS) pH 7.4 with Pi and PhosSTOP. The resulting solution was centrifuged at 120 000 g for 1 h (Beckman Optima XPN-80, SW32 Ti rotor). The pellet was then taken up in 10 mM PBS and centrifuged at 120 000 g for 1 h. The pelleted synaptic junctions were shock frozen in liquid nitrogen.

Sample preparation for shotgun lipidomics, endocannabinoid and sphingolipid analysis

Samples consisting of approximately 300 μg protein (25μl of aliquot) were used for lipid extraction as previously described by Coman et al. (2016). In brief, 225 μl MeOH was added to the sample, and three freeze-thaw cycles with intermediate ultrasonication were performed to homogenize the samples. Next, 750 μl of methyl-tert-butyl-ether (MTBE) and the internal standard mixture were added, and the samples were incubated for 1 h at 950 rpm and 4°C. To induce phase separation 188 μl water was added to the samples. After a centrifugation step of 10 min at 4°C and 10 000 g, the upper organic phase (containing PLs, SLs, CEs, and GLs) was carefully removed and dried under a gentle nitrogen flow whereas, to the lower aqueous phase, 527 μl methanol were added. Subsequently, the samples were stored at −20°C for 2 h to complete protein precipitation and centrifuged for 30 min at 13 500 g. The protein pellet was dried and further subjected to protein analysis and the dried organic phase was reconstituted for lipid analysis.

Shotgun lipidomics

A Q Exactive HF or a Plus mass spectrometer (Thermo Fisher Scientific) connected to a TriVersa NanoMate ion source (Advion Biosciences) was used to analyze the rat and mice samples, respectively. For the direct infusion experiments, 12 μl of sample, reconstituted in 150 μl IPA/MeOH/CHC_{l3} (4:2:1; v:v:v) containing 7.5 mM ammonium acetate, were delivered over 14 min with a backpressure of 0.95 psi. The voltage was set to 1.25 kV for 6 min and subsequently to −1.25 kV to acquire mass spectra in positive and negative mode in the same measurement. In both modes, full MS spectra covering the 350–1200 m/z range were acquired with a resolution of 240 000, an AGC target of 10^6 and a maximum IT of 105 ms for Q Exactive HF and a resolution of 140 000, AGC target 10^6 and a maximum IT of 100 ms for Q Exactive Plus. The MS1 acquisition of the rat P2, So and Sj samples was followed by a data independent acquisition (DIA) for precursor masses at an interval of 1.001 Da whereas for EE samples by a data dependent acquisition (DDA) of the 20 most intense signals. MS/MS spectra were acquired with a resolution of 60 000 and 35 000, an AGC target of 10^5 and a maximum IT of 105 and 200 ms for DIA and DDA, respectively. The precursor isolation window was 1 Da and the nCE was 21% and 24% for positive and negative mode, respectively.

Targeted sphingolipid analysis

Analysis of sphingolipids was performed as previously described by Peng et al. (2017). Briefly, an UltiMate 3000-system (Thermo Fischer Scientific, Darmstadt, Germany) was equipped with an Ascentis Express C18 main column (150 mm × 2.1 mm, 2.7 μm, Supelco) and fitted with a guard cartridge (50 mm × 2.1 mm, 2.7 μm, Supelco) in a column oven with a temperature of 60°C. Solvents and gradients were adapted (Peng et al., 2017). Solvent A was ACN/H2O (6:4, v:v; 10 mM AF, 0.1% FA, 5 μM PA), and solvent B was IPA/ACN (9:1; v:v; 10 mM AF, 0.1% FA, 5 μM PA). The separation was carried out at a flow rate of 0.5 ml/min with the following 25 min long gradient: initial (30% B), 0.0–2.0 min (hold 30% B), 2.0–3.0 min (30%–56.1% B), 3.0–4.0 min (56.1%–58.3% B), 4.0–5.5 min (58.3%–60.2% B), 5.5–7.0 min (60.2%–60.6% B), 7.0–8.5 min (60.6%–62.3% B), 8.5–10.0 min (62.3%–64.0% B), 10.0–11.5 min (64.0%–64.5% B), 11.5–13.0 min (64.5%–66.2% B), 13.0–14.5 min (66.2%–66.9% B), 14.5–15.0 min (66.9%–100.0% B), 15.0–19.0 min (hold 100% B), 19.0 min (5% B), 19.0–22.0 min (hold 5% B), 22.0 min (30% B), 22.0–25.0 min (hold 30% B). The LC system was coupled to a QTRAP 6500 (Applied Biosystems, Darmstadt, Germany). The measurements were performed in positive with the following ESI source settings: curtain gas 30 arbitrary units, temperature 250°C, ion source gas I 40 arbitrary units, ion source gas II 65 arbitrary units, collision gas medium; ion spray voltage +5500 V, declustering potential +100 V/–100 V, entrance potential +10 V, and exit potential +13 V. For the scheduled SRM, Q1 and Q3 were set to unit resolution. The scheduled SRM detection window was set to 2 min, and the cycle time was set to 0.5 s.

Targeted endocannabinoid analysis

Samples of the rat inventory were prepared as described above. Internal standard mixture solved in 250 µl MTBE was added after cell lysis. Endocannabinoids and endocannabinoid-like (eCB-like) were quantified with an external six-point calibration curve of pure eCB-like standards in matrix free solution. The organic phase (700 µl) was dried under a gentle nitrogen flow and the samples were reconstituted for LC-MS/MS analysis in 75 µl ACN/H2O/IPA (3.6:6:0.4, v/v/v) containing 0.1% FA and 5 mM AF. One microliter of the sample solution was injected on a nanoLC system equipped with 40 cm column (Polymicro Technologies) with 360 µm OD and 100 µm ID, self-packed with Supelco Ascentis Express C18 particles (2.7 µm particle size). Oven temperature was set to 60°C. Solvent A was H2O/ACN/IPA (60:36:4, v:v:v) containing 0.1% FA and 3 mM AF, solvent B was ACN/IPA (9:1, v:v) containing 0.1% FA and 3 mM AF. Gradient flow was set 0.6 µl/min. The gradient started by 1.0% B hold for 5 min, increased to 40% at 15 min followed by an increase to 68% at 32 min, and an increase to 99% at 55 min. Solvent B was hold for 10 minutes at 99% to a total run time of 65 min. The column was equilibrated to 99% solvent A for 25 minutes after the analytical run.

SRM experiments were conducted on a TSQ Vantage (Thermo Fisher Scientific) in positive ion mode with the following parameters: a cycle time of 1 s, and an average dwell time of 26 ms; the Q1 and Q3 were set to 0.70u (FWHM), emitter voltage was set to 1500 V, delustering potential 10, and the temperature of the transfer capillary to 275°C.

The Q Exactive HF instrument was configured to perform a survey scan and 8 PRM in one measuring cycle. Full scan settings were as follows: resolution of 240 000 (m/z 200), AGC of $1*10^6$ and maximum IT of 100 ms. For PRM, spectra were acquired as follows: isolation window of 0.4 m/z, mass resolution of 30 000, AGC of $5*10^5$ and maximum IT of 100 ms.

Sample preparation and phosphoinositide (PIP) analysis

For phosphoinositide (PIP) sample preparation and analysis to 10 µl of each P2, So and SJ homogenates, 725 µl $CHCl_3$/MeOH (1:2, v:v) was added and samples were sonicated in an ice-cold sonication bath for 1 min. To each sample, 170 µl H_2O, 25 µl 50 mM NaOH solution, PIP(4,5)-FP (200 pmol) as internal standard and 725 µl $CHCl_3$ were added. Subsequently, the samples were vortexed for 10 s, centrifuged at room temperature (RT) and 1 500 g for 5 min. The resulting lower phase was discarded and to the remaining sample containing the PIPs, 333 µL MeOH, 170 µL 2 M HCl and 667 µL $CHCl_3$ were added. Next, samples were allowed to stand at RT for 5 min with occasional vortexing and, after a centrifugation step at RT and 13 500 g for 5 min, the lower phase was collected and dried under a gentle stream of nitrogen. The protein pellet was stored for protein amount determination by BCA. Fatty acids were deacetylated by adding 50 µL of methylamine solution in H2O/MeOH/1-butanol (43:46:11, v:v:v) to the dried lipids extracts. The samples were incubated at 53°C for 50 min in a thermomixer at 1,000 rpm (Thermomixer Comfort; Eppendorf, Hamburg, Germany). The reaction was stopped by adding 25 µl of ice-cold IPA. Samples were dried under a gentle stream of nitrogen, reconstituted in 50 µl H_2O, and centrifuged prior to transfer to the injection vials.

PIP analysis was conducted on a HPLC−ESI-MS/MS setup using a Dionex ICS-5000 instrument (Thermo Fischer Scientific, Darmstadt, Germany) coupled to a Q Exactive HF (Thermo Fischer Scientific, Darmstadt, Germany) that was equipped with an electrospray ion source (HESI II). Chromatographic separation was accomplished on a Dionex IonPac AS11-HC column (250 mm × 2 mm, 4 µm particle size, Thermo Fischer Scientific) fitted with a guard column (50 mm × 2 mm, 4 µm, Thermo Fischer Scientific). A segmented linear gradient at a flow rate of 0.380 ml/min was used for PIP separation: initially, 15 mM KOH was held from 0.0 to 5.0 min followed by 15 to 25 mM KOH from 5.0 to 15.0 min, 50 to 65 mM KOH from 15.0 to 30.0 min, 100 mM KOH from 30.0 to 34.0 min, 10 mM KOH from 34.0 to 38.0 min, 100 mM KOH from 38.0 to 42.0 min for washing, and 15 mM KOH from 42.0 to 45.0 min for re-equilibration. To exchange potassium ions against protons before MS analysis, a 2 mm Dionex AERS 600 suppressor was operated with 95 mA. The temperature of the autosampler, column oven, and suppressor was set to 10, 30 and 20°C, respectively. 5 µL of each sample was injected onto the system. Additionally, MeOH was added as makeup flow at a low rate of 0.150 ml/min. The following ESI source parameters were used: sheath gas 50, auxiliary gas 14, sweep gas 3, spray voltage 2.75 kV, capillary temperature 270°C, s-lens RF level 45 and auxiliary gas heater 380°C. The Q Exactive HF instrument was configured to acquire a full MS spectra at 200-700 m/z with a resolution of 60 000, an AGC target of 10^6 and a maximum IT of 50 ms, followed by PRM in one measuring cycle. The PRM settings were resolution of 60 000, AGC target of $3*10^6$, and a maximum IT of 120 ms. To increase the sensitivity for PIP3, from minute 25.5 until the end of the acquisition, the PRM settings were change to: resolution 240 000, AGC target of $3*10^6$ and a maximum IT of 500 ms. For both PRMs, the default charge state was 2 and the isolation window 0.4 m/z. The total acquisition time was 35 min. The NCE value for each PIP class was predetermined from NCE optimization analysis of the standards through direct infusion. All measurements were performed in negative ion mode. PIPs were quantified with an external calibration curve of pure standards in matrix free solution.

Sample preparation and ganglioside analysis

For ganglioside extraction and analysis, the samples were homogenized in 3 mL of $CHCl_3$/MeOH (2:1, v/v) using an ultrasonic bath at 40°C for 15 min. Next, 600 µl water was added, and the samples were centrifuged at 3 000 g for 3 min at RT. The aqueous layer containing gangliosides was collected and dried under a gentle stream of nitrogen. The dried aqueous phase was reconstituted in 1 mL pure water and subsequently desalted by using Sep-Pak C18 SPE cartridges (200 mg) (Waters, Milford, MA, USA). Initially, the cartridges were cleaned 3 times with 1 mL of MeOH and equilibrated 3 times with water. Samples were loaded onto the column, washed 3 times with water and, finally, the gangliosides were eluted by three times 1 mL of MeOH. The eluate was dried under nitrogen flow and reconstituted in MeOH/H_2O/$CHCl_3$ (300:150:50, v/v/v).

For ganglioside analysis, an Agilent 1290 Infinity series (Agilent Technologies, Waldbronn, Germany) was coupled to a Xevo G2-XS QTOF mass spectrometer (Waters, Milford, MA, USA). Separation was achieved on an Ascentis Si column (150 mm x 2.1 mm, 3 μm particle size, Sigma-Aldrich) under the following conditions: flow rate 0.3 ml/min, injection volume 1 μl, column temperature 40°C and mobile phase gradient: 0 min at 12.3% B, 15 min at 22.1% B. Re-equilibration time was 15 min. Solvent A was ACN with acetic acid and solvent B was 10 mM aqueous ammonium acetate, pH = 6.1 adjusted with acetic acid. Data were acquired in negative ion mode using the typical resolving power 22 000 (full width at half-maximum) and the following ESI parameters: sampling cone 20 V, source offset 90 V, capillary voltage 1 kV, source temperature 150°C, drying temperature 500°C, cone gas flow 0.8 l/min and drying gas flow 17 l/min. The scan time was 0.5 s and the mass range was 500-2000 m/z. Leucine enkephaline was used as lock mass for all measurements.

Proteomics sample preparation

The protein pellet obtained after lipid extraction was first homogenized in a lysis buffer containing 1% SDS, 150 mM NaCl and 50 mM Tris, pH = 8.5. After a centrifugation step of 30 min at 4°C and 18 000 g, the supernatant was immediately transferred to a new tube and the protein concentration was determined by the BCA assay (Thermo Fisher Scientific, Bremen, Germany). The determined protein concentration was further utilized for normalization of the lipidomics experiments and proteomics sample preparation. Proteolytic digests were checked for complete digestion and normalized for TMT labeling after desalting by using monolithic column separation (PepSwift monolithic PS-DVB PL-CAP-PM, Dionex) on an inert Ultimate 30000 PLC (Dionex, Germering, Germany) by direct injection of 1ug sample. A binary gradient (solvent A: 0.1% TFA, solvent B: 0.08% TFA, 84% ACN) ranging from 5%–12% B in 5 min and then from 12%–50% B in 15 min at a flow rate of 2.2 ul/min and at 60°C, was applied. UV traces were acquired at 214 nm. The TMT experiment was designed in such a way that 3 biological replicates were used for each membrane fraction (P2, So and SJ). The same amount of each nine samples was taken based on the amount determined from the PepSwift column. The channel 127N,127C,128C represents the SJ; channel 129N,129C and 128N were used for the So fraction; and channel 130C, 130N, 131 were used for P2 respectively. Channel 126 was used for mixed sample. The amount of peptides for each channel labeling were the same. The median of all reporter ions for each channel was used for further normalization.

For the TMT-based proteomics analysis of the rat P2, So, and Sj samples, acetone was added in a ratio of 1:4 (sample:acetone, v/v), and the samples were incubated at 4°C overnight. The resulting pellet was resuspended in 8 M urea, 0.1% rapigest (in house-synthesized) and 50 mM TEAB buffer. The proteins were reduced and alkylated using TCEP (final concentration 10 mM) for 1 hour at 22°C and IAA (final concentration 40 mM) in the dark for 30 min, respectively. Next, 50 mM TEAB was added to ensure urea concentrations less than 1 M. The proteins were digested using a trypsin to protein ratio of 1:40 (w/w) at 37°C in a ThermoMixer (Eppendorf) at 650 rpm, overnight. Protein digestion was stopped by adding formic acid and the samples were centrifuged at 15 000 g for 10 min. The supernatant was desalted using C18 cartridges (Sep-Pak, 50 mg, Waters). Digestion efficiency was controlled by measuring 0.5 μg of each sample on a monolithic column. Afterward, the samples were dried again and resuspended in 100 mM TEAB buffer. The same amount of each digested sample (100 μg protein of total digestion) were reacted with the TMT reagent (TMT 10plex, ThermoFisher) in 100 mM TEAB buffer for 1 hour at 25°C in a ThermoMixer (Eppendorf) at 550 rpm. To quench the reaction, 5% hydroxylamine was added, and the samples were incubated for 15 min at 25°C. Finally, the samples were combined to generate a pooled sample after checking the TMT labeling efficiency on a Q Exactive HF. The remaining samples were processed using filter-aided sample preparation with minor modification. Briefly, the samples were diluted to 10 mM SDS using freshly prepared 8 M urea, 100 mM Tris, pH = 8.5 and loaded onto a spin filter by centrifugation for 15 min at 13 500 g. Afterward, samples were washed three times with 8 M urea, 100 mM Tris, pH = 8.5 and three times with 50 mM TEAB by centrifugation at 13 500 g for 15 min. Protein digestion was performed in 50 mM TEAB, 0.2 M GuHCl and 2 mM $CaCl_2$ using a trypsin to protein ratio of 1:20 (w/w) for 12 h at 37°C. Finally, peptides were eluted with 50 mM TEAB by centrifugation and acidified to 1% TFA. Digestion efficiency was controlled by monolithic reverse phase separation and samples were stored at −80°C until further analysis.

Label free proteomics analysis

The analysis was performed on an Ultimate 3000 RSLC system coupled to a Q Exactive HF mass spectrometer or an Orbitrap Lumos Fusion (Thermo Scientific, Darmstadt, Germany) for the inventory and environmental enrichment, respectively. Briefly, peptides were preconcentrated on an Acclaim C18 PepMap trap column (2 cm x 75 μm, 3 μm, 100 Å, Thermo Scientific) followed by separation on an Acclaim C18 PepMap main column (15 cm x 75 μm, 3 μm, 100 Å, Thermo Scientific) using a binary gradient (solvent A: 0.1% FA, solvent B: 0.1% FA in 84% ACN). The gradient increased linearly from 3% to 35% B at flow rate 250 nl/min over 120 min. For Q Exactive HF data acquisition, survey scans were acquired with a resolution of 60 000, an AGC target of $3*10^6$ and a maximum IT of 50 ms, and were followed by data-dependent MS/MS of the 15 most intense signals. For the MS/MS scans, resolution was set to 60 000, AGC value to $2*10^5$, maximum IT to 100 ms, dynamic exclusion was 30 s, isolation window was 0.4 m/z and NCE was set to 33%. The Orbitrap Lumos data were acquired with a resolution of 60 000, an AGC target of $4*10^5$ and a maximum IT of 50 ms for the survey scans, and a resolution of 30 000, an AGC target of $3*10^4$, a maximum IT of 150 ms and an isolation window of 1 m/z for MS/MS scans.

Label free proteomics data analysis

Label-free quantification was performed using Progenesis QI software version 4.1. Raw data were aligned in automatic mode. The exported peak lists were further searched using searchGui 1.14.4, X!Tandem (version 2015.12.15.2) and Mascot (version 2.4) against a concatenated target-decoy mouse database (downloaded from Uniprot June 2015 time, 16716 entries). Protein inference at 1% false-discovery rate (FDR) was performed by using PeptideShaker (version 1.04+). Mass tolerance was set to 10 ppm for precursor and 0.5 Da per fragment ion. Trypsin was set as protease with a maximum of two missed cleavages. Post-translational modifications were set as following: carbamidomethylation of cysteine as static modification and oxidation of methionine as variable modification. PeptideShaker output was reimported into Progenesis. Peptide-ion measurements were exported from Progenesis and processed by an in-house pipeline developed based on MSStats (Version 3.10.4) (https://doi.org/10.18129/B9.bioc.MSstats) R package. Only proteins with at least two unique peptides were considered for quantification. Peptide abundances were log2 transformed; missing values were censored and imputed. Preprocessed data were normalized based on quantile. Relative abundance of each protein per run was estimated by Tukey's median polish. Fold- change between standard and enriched environment conditions and p value were calculated per protein. Significantly changing proteins were determined based on p value < 0.05 threshold.

TMT-based proteomics data analysis

Data were analyzed using Proteome Discoverer version 2.1 (Thermo Scientific). For both, the reviewed and unreviewed rat proteome data were retrieved from Uniprot database (downloaded on 28 November 2018, 36076 entries). The MS and MS/MS data were searched against this database by using Mascot and Sequest search engines. A 10 ppm precursor mass tolerance was used, with 0.02 Da fragment mass tolerance on the Q Exactive HF mass spectrometer. Trypsin was set as the enzyme allowing maximum two missed cleavage. Carbamidomethylation of cysteine and TMT tags on peptides Lysine and any N terminus residues were searched as static modifications. Oxidation of methionine was searched as variable modification. The target-decoy approach was used to evaluate false-positive peptide-spectrum matches based on 1% false-discovery rate (FDR). Multiple test correction was performed by adjusting the calculated p values according to Benjamini-Hochberg. Proteins with an adjusted p value < 0.05 were classified as significant. All data analysis and plots were performed using R (Version 0.99.903).

Functional Annotation and Pathway Enrichment Analysis

We performed pathway enrichment analysis to determine the significantly enriched metabolic pathways that include significantly regulated proteins. The analysis was done by using ClueGO plugin (version 2.5.3) on open source network visualization platform Cytoscape (version 3.6.1). Kyoto Encyclopedia of Genes and Genomes (KEGG) (release 89.0) and Reactome databases (release 66) of corresponding organisms were downloaded, and an integrated database was curated. The p value of each pathway was computed using hypergeometric test and corrected by applying Benjamini-Hochberg. Pathway enrichment criteria were applied as follows: (1) An enriched pathway must include at least three proteins of query list. (2) At least one of the found proteins must be significantly regulated. (3) Enriched pathways were filtered based on p value < 0.05 for overrepresentation. Missing parent nodes were added externally based on the hierarchy of corresponding pathway database. The coverage of each pathway was computed, and the pathways related to neuronal development and signaling were further investigated. Lipid ontology annotations of significantly regulated lipids in enriched environment were performed by using LION server (*11*). Using all quantified rat hippocampal proteins, we performed pathway mapping to KEGG and Reactome databases using gprofiler2 R package (0.2.0). All mapped pathways regardless of deemed significancy were retrieved. Pathways which are directly or indirectly related to lipid metabolism were taken. The proteins which were found associated to these pathways were mapped to STRING protein-protein interaction network (PPIN). As interaction sources between proteins, we only kept interactions based on experiments, databases and/or neighborhood. We determined 0.8 as interaction confidence score. We grouped the proteins (circle shape) based on related lipid metabolism pathway (diamond shape). To these pathways, we also linked corresponding lipid species as additional nodes (rectangular shape). We differentiated the pathways based on color coding.

Transfections

Neurons were transfected with Lipofectamine 2000. For volume marker transfections neurons were transfected for 24 h before fixation. In knockdown experiments, neurons were transfected at DIV9 and fixed at DIV14 as described below. The knock down (KD) construct was generated by cloning the KD sequence into the PSI-HIV-H1 vector (System Biosciences). The shRNA is expressed under the H1 promoter, to identify transfected cells GFP was expressed under the CMV promoter in the same construct. For expression of GFP as a volume marker the EGFP-N1 vector (Clontech) was used. For labeling of the cell membrane Myristoylated Alanine-rich C-kinase Substrate (MARCKS) was fused to EGFP and cloned into a FUGW-plasmid (David Baltimore, addgene 14883) and expressed under the Ubiquitin promoter.

Treatments

All treatments were conducted in culture medium at 37°C, 5% CO_2 and 95% humidity. For silencing of primary culture, 1 μM TTX was added to the medium. For inhibition CB1R signaling, 10 μM AM-251 was added to the medium. Primary culture was stimulated by inhibiting inhibitory signaling using the GABA-receptor antagonist Bicuculline 50 μM.

Immunocytochemistry

Following fixation with 4% paraformaldehyde (PFA) and 4% sucrose for 10 min, cells were washed thoroughly three times with PBS and permeabilized with 0.2% Triton X-100 in PBS for 10 min. Cells were incubated with blocking buffer containing 2% Glycine, 2% BSA, 0.2% gelatine and 50 mM NH_4Cl for 1 h at room temperature (RT), for staining including ATTO dies for STED imaging, 10% horse serum with 0.1% Triton X-100 in PBS was used as the blocking buffer. Incubation with primary antibodies (Table S1) was done in blocking buffer at 4°C overnight. Coverslips were washed three times in PBS and incubated with the secondary antibodies (Table S1h) in blocking buffer and washed again three times with PBS. Coverslips were then rinsed in water and mounted with the self-hardening polyvinyl alcohol Mowiol (-CH_2CHOH)n (Carl Roth, Karlsruhe, Germany). For surface labeling, neurons were incubated with the primary antibody at 4°C in ACSF (artificial cerebrospinal fluid) (119 mM NaCl; 2.5 mM KCl; 2 mM $CaCl_2$; 2 mM $MgCl_2$; 30 mM glucose; 25 mM HEPES in H_20 at pH 7.4), washed in ACSF and then fixed and stained as described above. For surface labeling during stimulation, the surface antibody was added to the medium of the stimulated groups and the control groups 10 minutes before the end of the stimulation.

Ultrastructural analysis with transmission electron microscopy

Mice were deeply anaesthetized and transcardially perfused with a mixture of 4% PFA and 1% glutaraldehyde (GA) in 0.1 M phosphate buffer (PB) at pH 7.4. 100 μm thick vibratome sections from enriched environment and standard cage control mouse brains were cut with a Vibratome VT 1000S (Leica Biosystems Nussloch, Germany). The sections were rinsed three times in 0.1 M sodium cacodylate buffer (pH 7.2–7.4) and osmicated using 1% OsO4 in cacodylate buffer. Following osmication, the sections were dehydrated using ascending ethyl alcohol concentration steps, followed by two rinses in propylene oxide. Infiltration of the embedding medium was performed by immersing the pieces in a 1:1 mixture of propylene oxide and Glycidether 100 (Epon) (Carl Roth Karlsruhe, Germany) and finally in neat Epon and hardened at 60°C. Semithin sections (0.5 μm thick) from the hippocampus were cut with a diamond knife (Diatome, Nidau, Switzerland) at an EM UC7 Ultramicrotome (Leica Microsystems, Wetzlar, Germany) and mounted on glass slides for light microscopy after being stained for 1 min with 1% Toluidine blue. Ultrathin sections (60 nm) were examined in a transmission electron microscope (TEM) EM902 (Zeiss, Oberkochen, Germany). Images were acquired with a 4K digital camera (A. Tröndle, Moorenweis, Germany) in the stratum radiatum of the hippocampal CA1 region and in the mossy fiber region of the hippocampal CA3 region. To maximize the number of synapses analyzed, regions of interest (ROIs) were chosen in between the main dendrites. Synapses were identified by the following criteria: An electron dense zone is present at the postsynaptic membrane, small vesicles are present in the presynaptic compartment, and both are in juxtaposition to each other. Mitochondria were defined as double membrane structures containing parallel membrane stacks.

Immunohistochemistry (IHC)

Mice were deeply anaesthetized and transcardially perfused with 4% paraformaldehyde in 0.1 M phosphate buffer (PB) at pH 7.4. The brains were postfixed overnight at 4°C and subsequently cryo-protected in 0.5 M sucrose solution followed by 1 M sucrose solution. Brains were shock frozen for 30 s at −50°C in 2-methyl-butan and then transferred to −80°C. Brains were embedded in Tissue-Tek mounting medium and cryosections were cut 20−–40 μm thick at ∼-20°C. For staining including the FAAH antibody antigen retrieval was conducted by incubating the slices in 10 mM sodium citrate dehydrate at 80°C for 30 minutes. After cooling to RT, the slices were washed 3 times for at least 5 Minutes in PBS, before continuing with the staining protocol. The sections were washed three times in PBS, blocked in blocking buffer (10% normal goat serum (NGS) 0,3% Triton X-100 in PBS) for 4 h. The sections were incubated with the primary antibodies (S1H Data) in blocking buffer at 4°C for 48 h. The slices were subsequently rinsed in PBS and washed in PBS for 1 h followed by 1 h 0.2% BSA in PBS. They were then incubated with the secondary antibody in blocking buffer for 2 h, washed three times for 15 min in PBS and mounted in Mowiol.

Image acquisition

Images were acquired using a Leica SP8 microscope (Wetzlar, Germany) in sections from enriched environment and standard cage control animals. Stratum oriens, stratum lacunosum moleculare and stratum radiatum of the hippocampal CA1 region were imaged. Frames of 512 × 512 pixels (36.89 μm x 36.89 μm) were acquired, with a z-step size of 0.3 μm. Gated STED images were acquired with a Leica TCS SP8 STED 3X equipped with pulsed White Light Laser (WLL) and diode 405 nm laser for excitation and pulsed depletion with a 775 nm laser. A Leica HC APO CS2 × 100/1.40 oil objective was used. Images were taken as a single plane of 1024 × 1024 pixels and optical zoom of 5 with a pixel size of 18 nm.

Image analysis

The background was removed using the remove background function of the Fiji software (University of Wisconsin, USA), for purposes of representation a Gaussian blur with a sigma radius of 0.6 was applied to the representative images. Synaptic stainings were analyzed using OpenView software (written by Dr. Noam Ziv, Technion Institute, Haifa, Israel).

To quantify synapses, intensity maxima were detected automatically, and boxes of equal size were centered on each maximum. The mean fluorescence intensity was measured for each box in the channel of interest. For colocalization analysis the boxes from the first channel were transferred to the second channel and the match set function was applied. For triple Colocalization the boxes were transferred to the third channel and the match set function was applied again.

Immunoblotting and analysis

Immunoblots were quantified using the Gel function in Fiji. The resulting values were normalized to the corresponding loading control. These values were then normalized to the control group.

Acute hippocampal slice preparation and electrophysiology

Hippocampi from mice of standard or enriched environment housing were dissected into 350-μm-thick slices using a vibratome (LeicaVT1000S, Nussloch, Germany). Hippocampal slices were pre-incubated for 2 h in carbogenated (95% O2 ~5% CO_2) ACSF (110 mM NaCl; 2.5 mM KCl; 2.5 mM $CaCl_2$; 1.5 mM $MgSO_4$; 10 mM glucose; 27.4 mM $NaHCO_3$ in H_20 at pH 7.3) at RT. Once slice at a time was transferred into a slice recording chamber (Scientific systems Inc.) and allowed to recover for at least 30 min. Field excitatory postsynaptic potentials (fEPSPs) were evoked by stimulation of CA1 Schaffer-collateral with 0.9% NaCl filled glass capillary microelectrodes (3-5 MΩ). fEPSPs were recorded and amplified by an Extracellular Amplifier (EXT-02B, npi, Germany) and digitized at a sample frequency of 20 kHz by AD/DA converter (POWER 1401mkII, CED, England). The stimulation strength was adjusted to 30 - 40% of the maximum fEPSP-slope values. For basal recording a single biphasic stimulus (half-pulse width: 100 μs) was applied every 60 s and the resulting signals were offline averaged over 5 min. After a stable baseline recording, long term potentiation (LTP) was induced by either 100 Hz trains or theta-bursts. Following tetanization sequences were applied: Weak theta-burst stimulation consisted of five bursts with four stimuli (100 Hz) every 200 ms; or 8 theta-burst sequences every 30 s that had 10 bursts of five stimuli; or single 100 Hz tetanization that consisted of a 1 s 100 Hz train (100 stimuli, half-pulse width: 100 μs); or three repeated 1 s 100 Hz trains every 10 min (half-pulse width: 200 μs).

For Depolarization-induced suppression of inhibition (DSI), transverse 400 μm hippocampal slices of adult male mice were cut with a vibratome (Leica VT1000S) in ice-cold ACSF solution containing 124 mM NaCl, 4.9 mM KCl, 2mM $MgSO_4$, 2mM $CaCl_2$, 1.2mM KH_2PO_4, 25.6 mM $NaHCO_3$ and 20 mM glucose, equilibrated with 95% O_2/5% CO_2. Slices were incubated at 34 °C for 25 min and subsequently held at room temperature. Whole-cell patch-clamp recordings were performed in CA1 pyramidal neurons with a pipette containing: 131mM cesium gluconate, 1mM $CaCl_2$, 10 mM EGTA, 10 mM HEPES, 10 mM glucose, 5 mM ATP, 0.4 mM GTP (pH 7.25; 290 mOsm). IPSCs were evoked by monopolar stimulation through a pipette placed in stratum pyramidale of CA1. Recordings were done in the presence of NMDA and AMPA/KA receptor antagonists D-AP5 50 μM and CNQX 10 μM. Depolarization-induced suppression of inhibition (DSI) was induced by a 5-s step from -60 mV to 0 mV. IPSCs were recorded every 5 s with an EPC10 HEKA amplifier (Harvard Bioscience, Holliston, Massachusetts, United States).

QUANTIFICATION AND STATISTICAL ANALYSIS

Graphs and statistical analysis were made with GraphPad Prism (GraphPad Software). Statistical tests used are written in the figure legend of the corresponding experiment. The number of subjects considered for statistical comparison is described in graphs and/or figure legends associated with each experiment. The p values ≤ 0.05 were considered significant (*); $p \leq 0.01$ (**); $p \leq 0.001$ (***); $p \leq 0.0001$(****).